Endophilin BAR domain drives membrane curvature by two newly identified structure-based mechanisms

Michitaka Masuda[1,4], Soichi Takeda[2,3,4], Manami Sone[1], Takashi Ohki[1], Hidezo Mori[2], Yuji Kamioka[1] and Naoki Mochizuki[1,*]

[1]Department of Structural Analysis, National Cardiovascular Center Research Institute, Suita, Osaka, Japan, [2]Department of Cardiac Physiology, National Cardiovascular Center Research Institute, Suita, Osaka, Japan and [3]Laboratory of structural biochemistry, RIKEN Harima Institute at SPring-8, Mikazuki-cho, Sayo, Hyogo, Japan

The crescent-shaped BAR (Bin/Amphiphysin/Rvs-homology) domain dimer is a versatile protein module that senses and generates positive membrane curvature. The BAR domain dimer of human endophilin-A1, solved at 3.1 Å, has a unique structure consisting of a pair of helix–loop appendages sprouting out from the crescent. The appendage's short helices form a hydrophobic ridge, which runs across the concave surface at its center. Examining liposome binding and tubulation in vitro using purified BAR domain and its mutants indicated that the ridge penetrates into the membrane bilayer and enhances liposome tubulation. BAR domain-expressing cells exhibited marked plasma membrane tubulation in vivo. Furthermore, a swinging-arm mutant lost liposome tubulation activity yet retaining liposome binding. These data suggested that the rigid crescent dimer shape is crucial for the tubulation. We here propose that the BAR domain drives membrane curvature by coordinate action of the crescent's scaffold mechanism and the ridge's membrane insertion in addition to membrane binding via amino-terminal amphipathic helix.

Introduction

Membrane dynamics in a cell, such as membrane budding, tubulation, fission and fusion, is associated with changes in membrane curvature. The crystal structure of amphiphysin BAR (Bin/Amphiphysin/Rvs-homology) domain revealed an unexpected structural identity with arfaptin2, a binding protein to Arf and Rac small GTPases (Tarricone et al, 2001), and provided a common structural base for the sensing and the formation of positive curvature membrane by BAR-family proteins (Peter et al, 2004).

Endophilins are cytoplasmic proteins containing an N-terminal BAR domain and a C-terminal SH3 domain, and are involved in membrane dynamics (Schuske et al, 2003; Galli and Haucke, 2004; Wenk and De Camilli, 2004). There are five endophilin genes in the mammalian genomes, endophilin A1–3 and B1–2. Both A and B types are highly conserved from nematode to human. The most extensively studied one is endophilin-A1, a brain specific protein involved in clathrin-mediated synaptic vesicle endocytosis (Ringstad et al, 1997, 2001). Via SH3 domain, endophilins bind to the GTPase dynamin, a membrane scissor, and the polyphosphoinositide phosphatase synaptojanin, a clathrin-uncoater (Ringstad et al, 1997; de Heuvel et al, 1997; Verstreken et al, 2003). The BAR domain of endophilins is classified into the N-BAR subgroup characterized by a short amphipathic helical sequence preceding the consensus BAR-domain sequence (Peter et al, 2004). The N-BAR domain of endophilin-A1 binds to liposomes and induces the tubulation in vitro, requiring the short amphipathic helical sequence (Farsad et al, 2001).

The crescent-shaped BAR dimer structure implies a simple model to drive membrane curvature: the dimer may impress its positively charged concave surface on the negatively charged membrane to form a high-curvature membrane domain (Gallop and McMahon, 2005; McMahon and Gallop, 2005). This curvature-impressing or scaffold mechanism for membrane deformation is based on an assumption that the dimer behaves as a rigid body on the membrane (Zimmerberg and Kozlov, 2006). Although the essential requirement of positively charged residues on the concave surface has been suggested (McMahon and Mills, 2004; Peter et al, 2004), there have been no experimental supports for the scaffold mechanism. Here, we show the requirement of the molecular rigidity of the BAR dimer for membrane curvature on the basis of structure-oriented mutational analysis.

By determining the structure of endophilin-A1 BAR domain, we found a distinction from those of the known BAR domains: a helix–loop appendage of 30 amino acids stretch is inserted into the helix 1 of the canonical BAR domain. A pair of the helices of the appendages forms a hydrophobic ridge, which runs across the center of the concave surface of the dimer. We analyzed the function of this ridge as well as the previously proposed structure, the N-terminal amphipathic helix and the crescent main body, for membrane deformation (Peter et al, 2004). N-terminal amphipathic helix is essential for membrane binding. The crescent main body of the BAR dimer is required for impressing its intrinsic curvature to the membrane. The ridge contributes to deform the membrane

*Corresponding author. Department of Structural Analysis, National Cardiovascular Center Research Institute, 5-7-1 Fujishiro-dai, Suita, Osaka 565-8565, Japan. Tel.: +81 6 6833 5012; Fax: +81 6 6835 5461; E-mail: nmochizu@ri.ncvc.go.jp
[4]These authors contributed equally to this work

presumably by penetrating into the membrane. Our results illustrate how these three components coordinate to induce membrane deformation.

Results

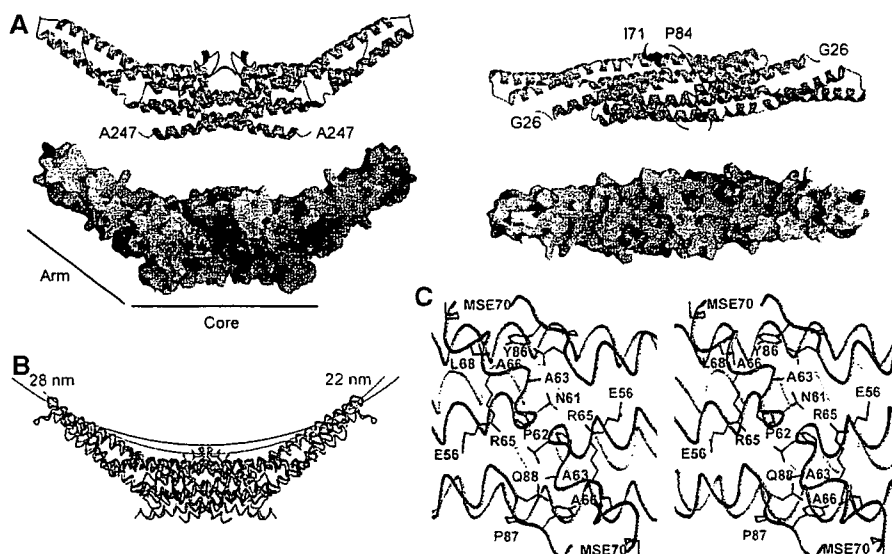### *Endophilin-A1 BAR domain has a unique appendage*

The structure of the BAR domain of human endophilin-A1 (amino acid 1–247, hereafter EndA1-BAR) was solved at 3.1 Å resolution by a multi-wavelength anomalous dispersion method. The structure of EndA1-BAR dimer is similar to that of amphiphysin (Peter *et al*, 2004) and arfaptin2 (Tarricone *et al*, 2001): a crescent-shaped dimer composed of a 6-helix bundle core and two 3-helix bundle arms extended from the core (Figure 1A). The whole structure of EndA1-BAR dimer can be precisely superimposed on that of amphiphysin and arfaptin (Figure 1B). All three structures show nearly identical dimer shapes. Notably, the present EndA1-BAR structure from a tetragonal crystal packing is almost completely the same as an independent crystal structure from an orthogonal crystal packing (Supplementary Figure 1; and Weissenhorn, 2005). The RMS deviations are 0.63, 0.86 and 0.80 Å for Cα atoms in monomers A, B and dimer, respectively. The structural identity indicates that the crescent shape is stably present in solution. Consistent with previous results (Habermann, 2004; Peter *et al*, 2004), structure-based sequence alignment reveals that these three proteins are poorly conserved in amino-acid sequence including the residues possibly important for the crescent-shape formation (Supplementary Figure 2).

We find a unique structure of the EndA1-BAR, an appendage-like structure protruded from the center of the dimer (Figure 1A). The sequence alignments of the BAR-family proteins indicated that this appendage appears unique to the endophilin-family proteins including nadrin (Habermann, 2004; Peter *et al*, 2004) and the candidates from yeasts (Supplementary Figure 2). The appendage (Q59–Q88) has an N-terminal short helix and a loop of which electron density is mostly missing (N72–G85). The pair of helices appears to stay on the main body and forms a ridge across the center of the concave dimer surface. The helix displays, on its top surface, a series of hydrophobic residues (P62, A63, A66 and M70) aligned 60° against the longitudinal axis of the dimer (Figure 1C). Other than the conserved hydrophobic amino acids of the ridge, the appendage sequences show clear distinction between endophilin-A and endophilin-B (Supplementary Figure 2). The B type endophilins show cytoplasmic localization, presumably being involved in intracellular membrane dynamics (Farsad *et al*, 2001; Modregger *et al*, 2003; Karbowski *et al*, 2004). Analyses of chimeric mutations in the appendage between EndA1-BAR and EndB1-BAR suggest that BAR domain may contribute to defining where to target, plasma membrane or intracellular organ membrane (Supplementary Figure 3).

### *The appendage's penetration enhances liposome tubulation*

To investigate the functional significance of the hydrophobic ridge of the endophilin-specific appendage, we first examined the effects of point mutations in this region (red residues in Figure 1C) on the liposome binding and tubulation activities *in vitro* (Figures 2A and 3). Introduction of membrane-repulsive negative charge (A66D) lost the ability to form tubes from liposomes. Hydrophilic mutations (A63S/A66S (SS) and A63S/A66S/M70Q (SSQ)) reduced the number of tubes (<1/100) and induced three-time enlargement of the tube diameter. In contrast, a bulky hydrophobic residue

Figure 1 Structure of human endophilin-A1 BAR domain dimer. (A) Ribbon representation (a green monomer with a red appendage and a pale-blue monomer with a blue appendage) and surface electrostatic potential (red, $-15\,kTe^{-1}$; blue, $15\,kTe^{-1}$) of the dimer viewed from the side (left) and from the top (right). The numbered amino-acid residues are the first and the last ones in consecutive polypeptide segments determined in this model. (B) Comparison of three BAR domain structures in trace representation. Red, endophilin-A1 (PDB ID: 1X03); green, amphiphysin (1URU); blue, arfaptin2 (1I4D). The red and green arcs with indicated diameters represent curved membranes fit the concave surface of endophilin-A1 and amphiphysin, respectively. (C) Stereo view of the appendages. Side-chains of the residues forming the hydrophobic ridge and those of interacting with residues of the main body are shown.

-421-
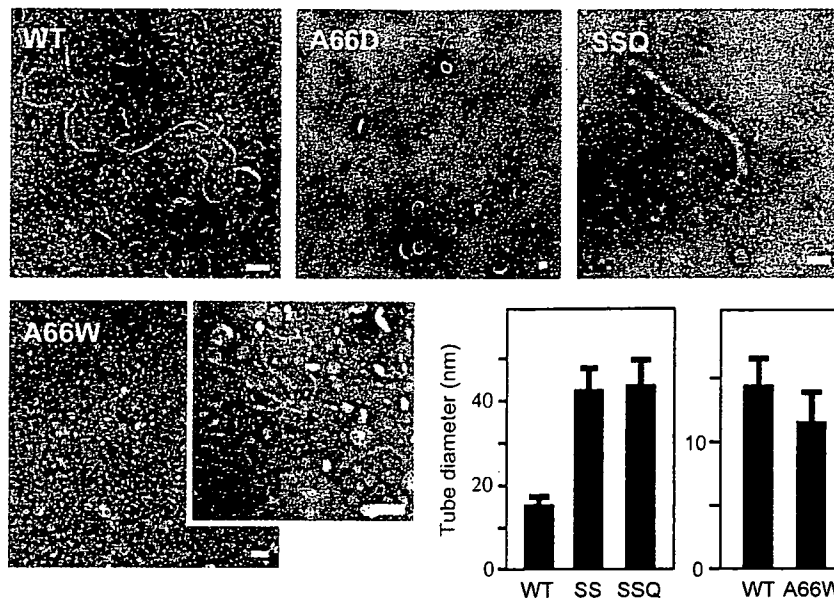
Figure 2 Liposome tubulation by endophilin-A1 BAR domains with mutations in the hydrophobic ridge. WT, 7 μM wild-type BAR domain incubated for 10 min; A66D, 28 μM, 10 min; SSQ, A63S/A66S/M70Q triple mutant, 28 μM, 10 min; A66W, 1.4 μM, 10 min (vesiculated, left panel) and 10 s (tubulated, right panel). Tubulation was not observed when incubated for longer than 1 min. Scale, 100 nm. The bar graphs show tubule diameter (mean and s.d.). SS, A63S/A66S double mutant, 28 μM, 10 min.
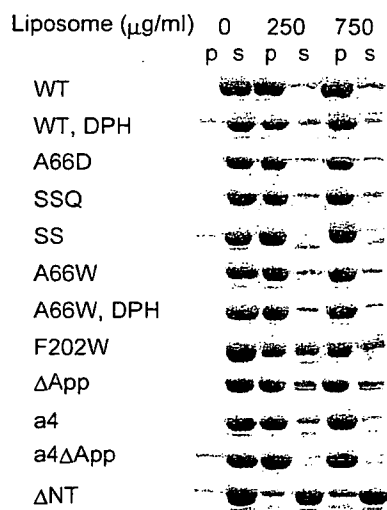
Figure 3 Liposome binding assays of endophilin-A1 BAR domain and its mutants. Protein (200 μg/ml) was co-sedimented with liposomes (0, 250 and 750 μg/ml). Proteins recovered from the pellet (p) and the supernatant (s) were analyzed by SDS–PAGE. The DPH-liposomes show similar binding capacity for the wild type (WT) and the A66W mutants. The liposome binding activity is slightly reduced in the F202W and the appendage-less mutants (ΔApp) and is almost lost in the helix 0 truncated mutant (ΔNT).

(A66W) led to extensive vesiculation and less tubulation. All these mutations did not affect the liposome binding. These results suggest an important role for the hydrophobic ridge in the membrane curvature formation but not in the membrane binding.

Although the ridge reduces the intrinsic curvature of the concave surface (red line in Figure 1B), it appears to promote the membrane curvature formation with conserved hydrophobicity. This raises the possibility that the ridge penetrates

into the membrane when the concave surface makes tight contact with the membrane. This possibility was investigated using tryptophan fluorescence, which is sensitive to hydrophobicity of the microenvironment around the indole moiety. The A66W mutant showed 10-nm blueshift of the fluorescence peak in a liposome-dose-dependent and saturable manner, while F202W, a control mutant in which Phe202 on the convex surface was mutated to Trp, did not show any shift (Figure 4A and Supplementary Figure 5). The amount of the blueshift was greater than that observed in 50% DMSO or 50% methanol, indicating that the indol moiety was in a highly hydrophobic environment.

To determine whether this blueshift was caused by the insertion of the indol moiety into the hydrophobic core of the lipid bilayer, we made fluorescence resonance energy transfer (FRET) assays using diphenyl-hexatriene (DPH) as the acceptor probe. DPH has been shown to insert specifically in the nonpolar interior of the membrane and not to alter the membrane structure and dynamics (Repáková *et al*, 2005). DPH liposomes did not affect liposome binding and tubulation (Figure 3 and Supplementary Figure 4). A66W but not F202W showed effective FRET from the 340-nm tryptophan fluorescence (donar) to the DPH fluorescence (acceptor) peaked at 430 nm (Figure 4B and C). It was not caused by changes in the fluorescence property of DPH itself possibly accompanied by tubulation/vesiculation of liposomes (Figure 4D and Supplementary Figure 6). These data suggest that the indol ring of 66W penetrates into the hydrophobic core of the membrane and that the remaining residues of the ridge, about 8 Å in height, appear to be embedded in the layer of lipid head-groups of the contacting membrane leaflet. These results confirmed that the ridge is contacting membrane and that the convex is not contacting membrane surface.

To provide further support for the membrane insertion of the ridge in the wild-type EndA1-BAR, we made a mutant
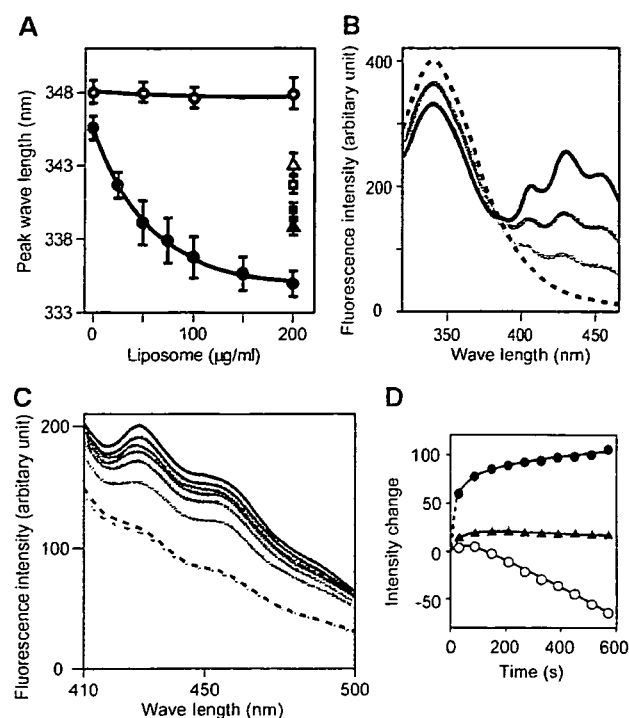
Figure 4 Tryptophan fluorescence blueshift and FRET assays. (A) Tryptophan fluorescence emission peak when excited at 280 nm was observed in different concentration of liposome. A66W (●), F202W control mutant (O), A66W alone in 50% DMSO (▲), in 50% MeOH (■), F202W alone in 50% DMSO (△), in 50% MeOH (□), 140 μg/ml protein for all measurements. Mean and s.d. ($N = 4$-11). The dose dependency is significant ($P \ll 0.001$) for the A66W mutant but insignificant ($P > 0.8$) for the F202W mutant (one-way ANOVA). DMSO and MeOH were used as blueshift inducer for tryptophan. (B) Dose-dependent FRET efficiency from the A66W tryptophan to DPH incorporated in liposomes was examined by the changes of fluorescence. Fluorescence spectrum of A66W (100 μg/ml) with the control liposome (200 μg/ml) excited at 280 nm (hatched). Pale to dark solid curves represent DPH:lipid weight ratios of 1:2000, 1:1000 and 1:500 in the same condition. (C) Time-dependent increase in the FRET efficiency from either A66W (pale to dark solid lines, from 30 to 570 s) or F202W tryptophan (pale and dark hatched lines, at 30 and 570 s) to DPH incorporated in liposomes. DPH:lipid weight ratio is 1:500. (D) The intensity changes at the 430-nm peak are plotted against time. A66W (●), F202W (▲) excited at 280 nm and A66W (O) excited at 360 nm.

with amphiphysin/arfaptin shape and examined its tubulation activity. The mutant (ΔApp), in which the entire appendage (Q59–Q88) was replaced with a helical stretch (AHLSSLLQ) derived from arfaptin2 sequence (A152–Q159, Y155S), show the crystal structure of a canonical BAR-domain dimer as designed (Figure 5A and Supplementary Figure 7). The ΔApp could bind to liposomes (Figure 3) and cause tubulation to a lesser extent than the wild type and amphiphysin-BAR (Figure 5D and Supplementary Figure 4). As the diameter of the tubules reflects the membrane curvature if the section of the tube is circle, we measured the diameter of the tube to compare the curvature of the EndA1-BAR and its mutant-induced tubes. Despite the higher curvature of the concave surface, the ΔApp dimer induced larger diameter tubules than the wild type did, indicating a positive contribution of the wild-type hydrophobic ridge to drive membrane curvature. Taken all together, the hydrophobic ridge penetrates into the interfacial leaflet of the lipid bilayer

when the concave surface is in contact with the membrane and promotes membrane curvature formation.

The BAR domain is rigid enough to impose its intrinsic curvature on membrane

A simple model for the concave surface-driven mechanism is that each BAR domain dimer acts as a molecular mold that impresses its curved surface on the membrane. This model suggests that the membrane curvature approximately mirrors the curvature of the concave surface. Indeed, the diameters of tubules induced by amphiphysin, ΔApp (Figure 5D), SS and SSQ mutants (Figure 2) are compatible with the model-based prediction (see Supplementary Table II for statistical analysis). However, this model has an assumption that the dimer should be rigid enough to overcome the bending resistance of the membrane (Nossal and Zimmerberg, 2002; Farsad and De Camilli, 2003). To examine whether the molecular mold mechanism is feasible, we developed a straight BAR domain by inserting one helical pitch into the helix II in the proximal portion of the extending arm (QSAL is inserted between I154 and Q155). This mutation (a4) would compensate the unequal lengths between helix II and III in the arm, a common feature of the known BAR domain structures, and let the curved arm into a straight one. Although the a4 mutant was designed simply to straighten the curvature of the domain, the structure solved at 2.4 Å resolution shows that it actually has the very interesting property of a flexible arm rather than a rigid one (Figure 5B). Four monomers in the asymmetrical unit show deviation in the bending angles of arms. The blue and the green monomers have straight arms while the orange monomer shows a bending pattern similar to the wild type and the yellow monomer is an intermediate. The structural deviation almost exclusively occurs in the helix kink regions (Supplementary Figure 8), indicating that the arm can swing at least from the bend-free straight position to nearly the wild-type position.

The a4 mutant allowed us to examine how flexibility of the crescent-shaped main body of the BAR dimer affects membrane curvature formation. The insertion of one helical pitch slightly distorts relative position of the helix II and III (Figure 5C), but does not largely rearrange the spatial positions of the residues on the concave surface of the arm (Supplementary Figure 8). Indeed, the a4 mutant and its appendage-lacking derivative (a4ΔApp) retained normal liposome binding activity (Figure 3). The a4 mutant vesiculated liposomes without any tubulation, while a4ΔApp lost these membrane-deforming activities (Figure 5D and Supplementary Figure 4). The concave surface-induced membrane deforming activity appeared to be lost in the a4 mutant, while the appendage's membrane insertion remained active. These results suggested that the rigidity of the crescent dimer structure is essential for liposome tubulation but not for vesiculation, although appendage insertion induces the vesiculation.

Roles for the amphipathic helix 0 of the N-BAR domain

The structure of a short amphipathic helix (helix 0) characterizing the N-BAR (Peter et al, 2004) can be resolved in the a4 mutant structure due to its tight crystal packing (Figures 5B and 6). The helix 0 is disordered in the wild type (Figure 6) and the ΔApp structures. The helix 0 has been

-423-
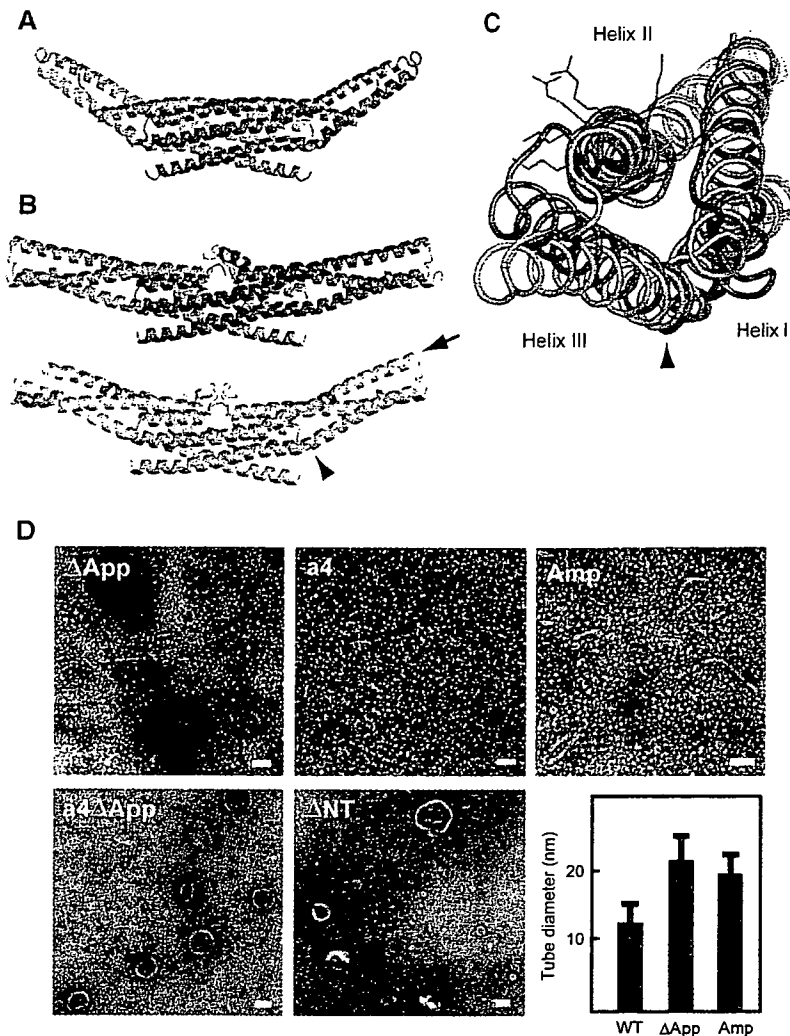
Figure 5 Distinct liposome tubulation induced by endophilin-A1 BAR domain mutants. (A) Ribbon representation of a mutated EndA1-BAR dimer lacking the entire appendages (ΔApp, PDB ID: 1X04). The entire appendage (Q59–Q88) was replaced with a helical stretch (AHLSSLLQ) derived from arfaptin2 sequence (A152-Q159, Y155S). Red, mutated segment. (B) Ribbon representation of the a4 mutant with swinging arms (PDB ID: 2D4C). One helical pitch was inserted into the helix II in the proximal portion of the extending arm (QSAL was inserted between I154 and Q155). Two dimers in the asymmetrical unit are shown separately. Red, inserted segment; magenta, helix 0. The bending patterns of the helix II and III varies among four monomers. An obvious kink in the helix III remains in the orange monomer (arrowhead, also in (C)). The residual curvature in the blue–green dimer is provided by the intersection of the monomers. (C) Superimposition of the a4 mutant monomer (orange one in (B)) and the wild-type monomer (blue) in the core region. A view from the distal end along the helix II (arrow in (B)) shows the maximum structural difference in these arms. Side chains of K171, 173 and R174 are shown. The helix III rotates 12° counterclockwise and shift 6 Å relative to the helix II at the distal end of the arm. The helix 0 and the core region are omitted. (D) Negatively stained liposome tubules induced by the BAR domains of endophilin mutants and amphiphysin. ΔApp, 7 μM, incubated for 10 min; a4, 7 μM, 10 min; a4ΔApp, 28 μM, 10 min; ΔNT, 21 μM, 10 min; Amp, 7 μM, 10 min. Note that a4, a4ΔApp, and ΔNT do not induce liposome tubulation. Scale, 100 nm. The bar graph shows tubule diameter (mean and s.d.).

suggested to be helical only when the amphiphysin BAR domain binds to liposomes (Peter *et al*, 2004). The helix 0 displays the hydrophobic branch of T14, V17 and V21 on one side, while K12, K16 and E19 on the other side (Figure 6). The helix 0 is connecting with the Helix I by a flexible linker G23–G24–A25. Consistent with the previous report (Farsad *et al*, 2001), truncation of the helix 0 (ΔNT) resulted in loss of liposome binding activity (Figure 3) and consequently abolished the tubulation (Figure 5D). In contrast, all the helix 0-containing mutants, including the A66D and the a4ΔApp showed intact liposome binding activity irrespective of their tubulation or vesiculation activities. These results indicate that the helix 0 in the endA1-BAR is critical for liposome binding and that the membrane binding of endA1-BAR via helix 0 is not sufficient to induce tubulation or vesiculation.
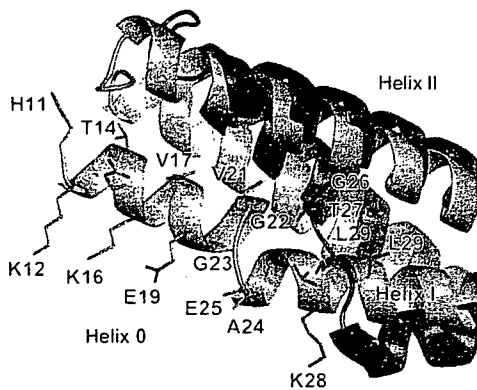
BAR domain induces tubular membrane deformation in vivo

To explore the significance of the helix 0, the rigid crescent mold, and the appendage of endophilin-A1 BAR domain *in vivo*, we further examined the membrane deformation activity of endophilin-A1 BAR domain in cells (Figure 7). Human umbirical vascular endothelial cells (HUVECs) expressing endophilin-A1 lacking SH3 domain (residues 1–296, hereafter, EndA1-BAR296), which was C-terminally tagged with enhanced green fluorescence protein (EGFP), exhibited intracellular fibrous structure similar to those induced by other BAR domain-containing molecules (Kamioka *et al*, 2004; Itoh *et al*, 2005). Notably, these structures developed from the periphery toward the center of the cells dynamically and disappeared reversibly in living cells (Figure 7E and

Supplementary Movie 1). Furthermore, these GFP-marked structures were co-localized with *in vivo* biotin-labeled membrane (Figure 7D), indicating that EndA1-BAR296-induced fibrous structure seems to be a membrane invagination originated from the plasma membrane. These structures were found in other cells we tested (Figure 7C). In clear contrast, ΔApp, ΔNT and a4 were incapable of inducing membrane deformation in cells, indicating the importance of helix 0, the rigid crescent shape, and the appendage of BAR domain for membrane deformation *in vivo*.

Discussion

The endophilin-A1 BAR domain dimer consists of three sub-modules: the crescent-shaped main body, the helix 0 and the unique appendage. We tried to understand the functional roles for these sub-modules in the membrane curvature formation. In this study by determining the structure of

endopholin-A1 BAR domain and developing mutants that were critical for the sub-module structure, we have explored the roles of sub-modules.

Here, we show that the structural rigidity of the crescent-shaped main body is critical for membrane tubulation. The BAR dimer is sufficiently rigid to overcome the bending resistance of the membrane and to be scaffolds for the tubulation (McMahon and Gallop, 2005; Zimmerberg and Kozlov, 2006). The insertion of one helical-pitch into the helix II at distal to the kink brings flexibility to the dimer (a4 mutant). The relative position of the three helices in the
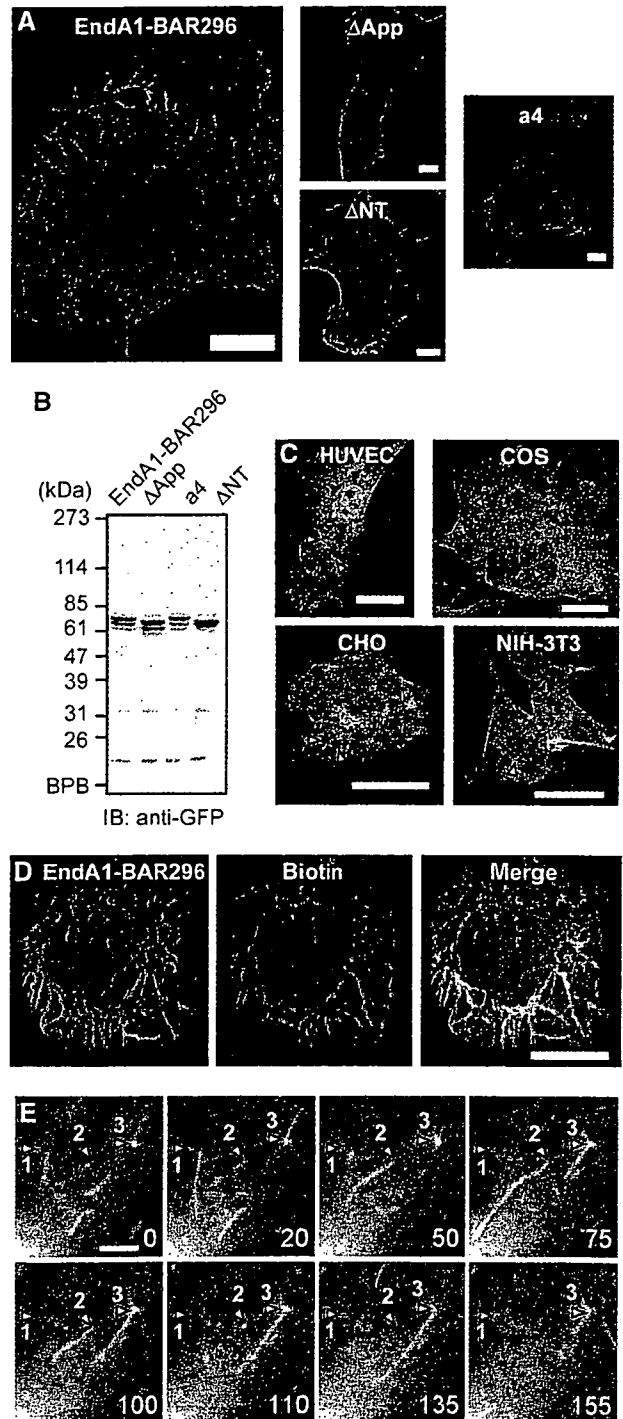

Figure 6 Close-up of helix 0 in an a4 mutant monomer (orange). The same superimposition as in Figure 5C but viewed from the side and displays the helix 0. The helix 0 is disordered in the wild-type structure (blue). The side chains of N-terminal residues are shown (H11KATQKVSEKVGGAEGTKL29 in the a4 and G26TKL in the wild type). The amphipathic helix 0 is stabilized by hydrophobic interactions with the helix II and III and also by hydrogen bonds with a symmetrical molecule.

Figure 7 Endophilin A1 BAR domain induces membrane tubulation *in vivo*. (A) HUVECs were transfected with plasmids expressing C-teminally EGFP-tagged EndA1-BAR296 (amino acid 1–296 of endophilin-A1), ΔApp, a4, and ΔNT. Cells were GFP-imaged on an epifluorescence microscope (Olympus IX-71). Fibrous structures were observed exclusively in EndA1-BAR296-expressing cells. Scale, 10 μm. (B) Protein expression of the EndA1-BAR296 and the mutants tagged with EGFP in transfected 293T cells were examined by immunoblotted with anti-GFP antibody. (C) Cells indicated were similarly transfected to (A). Arrowheads indicate the fibrous structures. Scale, 20 μm. (D) Live HUVECs expressing EGFP-tagged EndA1-BAR296 were biotinylated with sulfo-NHS-biotin for 10 min and chased for further 10 min. Covalently bound biotin was visualized using Alexa633-streptavidine. Fluorescence images for EGFP (left), Alexa633 (center), and merge (right) are shown. Scale, 10 μm. (E) A time lapse images of HUVECs expressing EGFP-tagged EndA1-BAR296 were obtained at the time point (seconds) after the observation (Supplementary Movie 1). EGFP-marked structure grows from the cell periphery towards the center of the cell. Notably, both extension and retraction of GFP-marked structure is observed (numbered arrow heads indicate each extending/retracting structure). Scale, 5 μm.

©2006 European Molecular Biology Organization

-425-

mutant arm was not changed in a4 mutant irrespective of the bend levels (Supplementary Figure 8). The mutant arm behaves as a rigid body and its structure changes only in the vicinity of the helix kinks when it swings. Therefore, it is unlikely that the flexibility of the mutant dimer can be a result of weakened inter-helix interactions in the arm. Moreover, we could not find any specific structural features in the kink region that might explain the flexible hinge in the swinging-arm mutant as well as the rigid bend in the wild-type BAR dimers of endophilin, amphiphysin, and arfaptin.

In this study, for the first time we could determine the structure of the N-terminal amphipathic helix (helix 0) using a swinging-arm mutant. Our mutant and previous mutation analyses indicated that the N-terminal helical sequence of endophilin-A1 is indispensable for liposome binding (Farsad *et al*, 2001), whereas that of amphiphysin is important but not essential for liposome binding and tubulation (Peter *et al*, 2004). The BAR domain of endophilin-A1 is an acidic polypeptide and the cluster of positive charge at the distal end of the arm is not prominent (Figure 1A). This property can explain the critical role for the helix 0 of the EndA1-BAR in liposome binding by providing additional basic residues. The helix 0 structure suggests that K12, K16 and possibly K8 are in a suitable position for cooperation with the positive charge cluster at the distal end. The amphipathic nature of the helix 0 implies that it can also insert into the membrane and facilitate the membrane curvature formation (Peter *et al*, 2004; Gallop and McMahon, 2005; McMahon and Gallop, 2005). Loss of the membrane-deforming activities of the A66D mutant (Figure 2) and the a4ΔApp mutant (Figure 5D) accounts for the additional mechanism for membrane deformation in addition to the membrane insertion of the helix 0.

The N-BAR of endophilins has one additional step to tubulate membrane. Here, we show that the hydrophobic ridge of the endophilin-specific appendage is inserted into the contacting membrane surface. Our data suggested that the entire ridge of the wild-type BAR domain, about 8 Å in height, is embedded in the layer of lipid head-groups of the contacting membrane leaflet. The embedding of the ridge into the membrane is consistent with the local spontaneous curvature mechanism that is reported very recently (Zimmerberg and Kozlov, 2006). As a protruding structure found in epsin1 induces liposome tubulation by being inserted to one leaflet of the lipid bilayer (Ford *et al*, 2002), the penetration of the hydrophobic ridge can drive the positive curvature by causing asymmetrical expansion of the surface area between two leaflets as shown in Figure 8 (Farsad and De Camilli, 2003).

We further explored the importance of the ridge, rigid crescent shape, and helix 0 in cells. We for the first time showed that N-BAR domain induced membrane invaginations originated from plasma membrane, although other BAR-containing molecules have been reported to induce similar invaginations (Itoh *et al*, 2005). Neither mutant that lacked either the ridge or the helix 0 nor flexible mutant formed the tubular invaginations in cells, indicating the significance of these sub-module structure in cells as suggest by *in vitro* studies. We constructed a series of endorphin-A1-EGFP expression plasmids to delineate the domain for the membrane invagination. Full-length endophilin-expressing cells did not show any tubular formation. Because endophilin consists of BAR domain and an SH domain, SH3-binding molecule such
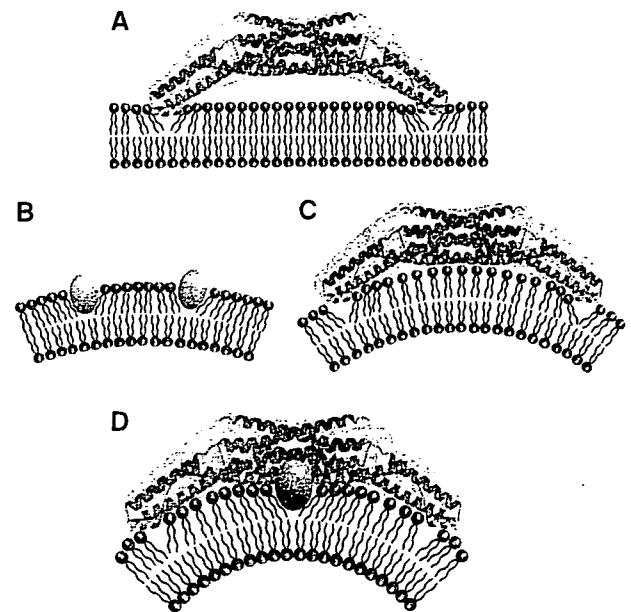
Figure 8 Two potential mechanisms for driving membrane curvature by endophilin-A1. (A) Kissing adhesion of an N-BAR domain on planar lipid bilayer. The helix 0 is essential for the membrane binding. Membrane insertion of the helix 0 is supposed. (B) Insertion of hydrophobic portions of macromolocules into one leaflet can create bilayer surface discrepancy that causes membrane curvature. (C) The simple N-BAR domain, such as amphiphysin and ΔApp, induces membrane curvature by impressing the concave surface onto the membrane. The rigidity of the molecule is required for this mechanism. (D) To drive membrane curvature, the endophilin N-BAR domain uses both the rigid crescent shape-mediated deformation and the insertion of hydrophobic ridge on the concave surface in addition to kissing adhesion of N-BAR to membrane surface.

as dynamin may inhibit the extension of membrane invagination. This possibility has been suggested in the membrane invagination found in FBP17 and amphiphysin (Kamioka *et al*, 2004; Itoh *et al*, 2005).

Collectively, EndA1-BAR uses two newly identified mechanisms to drive positive membrane curvature in addition to the essential binding capacity of helix 0 to the membrane: one by the scaffold mechanism common to the BAR domains and the other by the local spontaneous curvature mechanism caused by the membrane insertion of the ridge (Figure 8D). The ridge, which occupies the bottom of the concave lipid-binding surface, may not work until the main body of the BAR dimer localizes itself to a curved membrane. The ridge then inserts into the bilayer roughly perpendicular to the main body, and thus both deformations will occur in the same direction.

Materials and methods

-426-

sequence of GPLGS at the N-terminus. EndA1-BAR proteins except for F202W and a4 mutants were purified by crystallization during Prescission protease cleavage. The method, crystallization by regulated cleavage of large hydrophilic tag (CRECLE), was as follows. Purified GST fusions were concentrated to 20–30 mg/ml in an elution buffer (20 mM glutathione, 100 mM Tris-HCl, pH 8.0, 10 mM DTT, 1 mM EDTA, 1 mM EGTA) and then cleaved by a low concentration of prescission protease (1 U/mg protein or less) at 4°C. Slow increase in the tag-free protein concentration might be suitable for crystallization and more than a half of EndA1-BAR protein could be recovered as 20–100 μm microcrystals. They were washed with a low-salt buffer (20 mM HEPES, pH 7.4, 2 mM DTT, 0.2 mM EDTA, 0.2 mM EDTA) and resolved into a high-salt buffer (350 mM NaCl in the low-salt buffer) and used for further analyses.

Protein crystallization
Seleno-methionine (S-Met) derivatives of the EndA1-BAR domain and its appendage-less mutant (ΔApp) were produced in B834(DE3)pLysS cells using Overnight Express Autoinduction System 2 (Novagen). To make X-ray grade crystals in a cryo-ready condition, modified high salt buffer (50 mM HEPES, pH 7.4, 300 mM NaCl, 100 mM KI, 28% ethylene glycol, 5% glycerol, 25 mM DTT) was used. Crystals of 1 mm size were formed by dialysis against 50 mM CHES, pH 9.5, 260 mM NaCl, 28% ethylene glycol, 5% glycerol, 25 mM DTT, 0.4% benzamidine · HCl at 4°C and were flush frozen at 100 K. Crystals could also be grown by vapor diffusion from a similar protein solution using distilled water as the bath solution. The crystals were equilibrated in 50 mM HEPES, pH 7.4, 150 mM NaCl, 25 mM DTT, 0.4% benzamidine · HCl, 5% PEG 8000 and the saturated amount of xylitol as a cryoprotectant. Some of the crystals were soaked with 0.5 mM oleoyl-L-α-lysophosphatidic acid (Sigma) or malonyl-CoA (Sigma) for 4 days with daily change for the substrates. The a4 mutant crystals were grown by sitting-drop vapour diffusion using a bath solution containing 100 mM HEPES, pH 7.2, 200 mM calcium acetate, 10 mM DTT and 20% (w/v) PEG3350 at 20°C and then flush frozen after brief immersion in the same solution containing 16% DMSO. The wild type and the ΔApp mutant crystals belong to the same space group $I4_1$ and contain one monomer molecule in the asymmetric unit (Supplemental Figure 1). The a4 crystal belongs to $P2_1$ and contains two dimers in the asymmetric unit.

Structural determination
The EndA1-BAR structure was determined using the multiple anomalous dispersion (MAD) method. Multiple-wavelength X-ray diffraction data sets were collected from a single Se-Met crystal (crystal I) at SPring-8 beamline BL44B2 (Supplementary Table I). Single wavelength data sets of another crystal (crystal II) and of a ΔApp crystal used for the refinement were collected at BL45PX. The data set for the a4 mutant was collected at BL38B1. All diffraction data sets were collected at 90 K and were processed using HKL2000 suite (Otwinowski and Minor, 1997). The seven positions out of 10 expected selenium atoms were identified by SOLVE (Terwilliger and Berendzen, 1999). The initial phases calculated by SOLVE with a figure of merit of 0.59 at 3.2 Å resolution were further improved by RESOLVE (Terwilliger, 1999). The density modified MAD map (Supplementary Figure 1) had sufficient quality to trace the polypeptide chain except for the N-terminus and the loop region of the appendage. The model was built with TURBO-FRODO (Roussel and Cambillau, 1996) and refined to the resolutions of 3.1 Å by CNS (Brunger *et al*, 1998). The final model includes 210 residues (residues 26–71 and 84–247), and has an R factor of 23.6% (R_{free} of 26.4%). The ΔApp structure was solved by molecular replacement by MOLREP in the CCP4 suite (CCP4, 1994) and refined to the resolution of 2.9 Å by CNS. The simulated annealing omit electron density map calculated by CNS confirmed the continuous α-helical structure of the replaced region as designed (Supplementary Figure 7). The final model includes 200 amino-acid residues and has an R factor of 23.8% (R_{free} of 26.9%). The a4 mutant structure was solved by molecular replacement using the central core of the EndA1-BAR as a starting model and the arms were manually built (Supplementary Figure 7). The structure was refined to the resolution of 2.4 Å by CNS with an R factor of 21.5% (R_{free} of 26.9%). Main-chain dihedral angles of all non-glycine residues of these three models lie in allowed regions of the Ramachandran plot, with 94.3% for the EndA1-BAR, 94.1% for the

ΔApp mutant, and 96.4% for the a4 mutant in most-favored regions, respectively. Graphical representations were prepared using the programs TURBO-FRODO, MOLSCRIPT (Kraulis, 1991), RASTER3D (Merritt and Bacon, 1997), GRASP (Nicholls *et al*, 1991) and Pymol (DeLano, 2002).

Liposome binding and tubulation assays
Liposome sedimentation assay and tubulation assay were as earlier described (Peter *et al*, 2004 see also McMahon lab protocols: http://www2.mrc-lmb.cam.ac.uk/NB/McMahon_H/group/techniqs/techniqs.htm) with slight modifications. Briefly, Folch fraction 1 (Sigma) was used as the lipid source and liposome suspension, 1 mg/ml in liposome buffer (20 mM HEPES, pH 7.4, 150 mM NaCl, 1 mM DTT) was made by sonication. Freshly purified BAR domain proteins were diluted at about 1 mg/ml in the liposome buffer and ultracentrifuged at 400 000 g for 10 min just before use. No crystallization occurred at this or lower concentrations. For sedimentation assays, 20 μg proteins were mixed with 25 or 75 μg liposomes in 100 μl of the liposome buffer, incubated for 10 min on ice and ultracentrifuged at 200 000 g for 10 min. For tubulation assays, 400 μg/ml proteins were mixed with an equal volume of 400 μg/ml liposomes, left for 10 s to 30 min at room temperature, and then processed for negative staining. Judging from the liposome sedimentation and the tryptophan fluorescence assays, this protein to lipid ratio ensured nearly saturated protein–liposome binding. Magnification was calibrated using a grating replica of 2160/mm.

Tryptophan fluorescence and FRET assay
Fluorescence emission spectra were recorded with a Hitachi F-4500 fluorescence spectrophotometer (Ohki *et al*, 2004). For tryptophan fluorescence assays, 140 μg/ml tryptophan-containing mutants were mixed with 0–200 μg/ml liposomes in the liposome buffer, incubated for 3 min, and excited at 280 nm. For FRET assays, DPH-liposomes were made by adding DPH (Molecular Probe) into lipid solution (1:500 to lipid, w:w). The fluorescence of DPH-liposomes (200 μg/ml) excited at 280 nm was scanned from 400 to 500 nm at 1-min intervals. The first measurement of the 430-nm DPH peak was obtained at about 30 s after mixing with mutant proteins (100 μg/ml).

Cell culture, transfection and surface biotinylation
HUVECs were purchased from Kurabo and cultured in HuMedia-EG2 as described previously (Sakurai *et al.*, 2006). 293T cells, CHO cells, Cos7 cells, and NIH-3T3 cells were cultured in DMEM supplemented with 10% fetal bovine serum as described previously (Kamioka *et al.*, 2004). Cells were transfected using LipofectAMINE 2000 (Invitrogen). Live HUVECs were biotinylated with 5 mM sulfo-NHS-biotin (Pierce) in Opti-MEM (Invitrogen) for 10 min. They were washed once with Opti-MEM and chased for 10 min with the normal culture medium, and fixed with 2% formaldehyde after a brief wash with Opti-MEM containing 1/20 volume of Avidin D blocking solution (Vector Laboratory) to reduce the cell surface background staining. HUVECs were permeabilized with cold MeOH and biotin was visualized using Alexa633-streptavidine (Molecular Probe).

-427-

References

Brunger AT, Adams PD, Clore GM, DeLano WL, Gros P, Grosse-Kunstleve RW, Jiang JS, Kuszewski J, Nilges M, Pannu NS, Read RJ, Rice LM, Simonson T, Warren GL (1998) Crystallography & NMR system: a new software suite for macromolecular structure determination. *Acta Crystallogr D* **54:** 905–921

Collaborative Computational Project Number 4 (1994) The CCP4 suite: programs for protein crystallography. *Acta Crystallogr D* **50:** 760–763

DeLano WL (2002) *The PyMOL User's Manual*. DeLano Scientific: San Carlos, CA, USA

Galli T, Haucke V (2004) Cycling of synaptic vesicles: How far? How fast!. *Sci STKE* **2004:** re19

Farsad K, Ringstad N, Takei K, Floyd SR, Rose K, De Camilli P (2001) Generation of high curvature membranes mediated by direct endophilin bilayer interactions. *J Cell Biol* **155:** 193–200

Farsad K, De Camilli P (2003) Mechanisms of membrane deformation. *Curr Opin Cell Biol* **15:** 372–381

Ford MG, Mills IG, Peter BJ, Vallis Y, Praefcke GJ, Evans PR, McMahon HT (2002) Curvature of clathrin-coated pits driven by epsin. *Nature* **419:** 361–366

Gallop JL, McMahon HT (2005) BAR domains and membrane curvature: bringing your curves to the BAR. *Biochem Soc Symp* **72:** 223–231

Habermann B. (2004) The BAR-domain family of proteins: a case of bending and binding. *EMBO Rep* **5:** 250–255

de Heuvel E, Bell AW, Ramjaun AR, Wong K, Sossin WS, McPherson PS (1997) Identification of the major synaptojanin-binding proteins in brain. *J Biol Chem* **272:** 8710–8716

Itoh T, Erdmann KS, Roux A, Habermann B, Werner H, De Camilli P (2005) Dynamin and the actin cytoskeleton cooperatively regulate plasma membrane invagination by BAR and F-BAR proteins. *Dev Cell* **9:** 791–804

Kamioka Y, Fukuhara S, Sawa H, Nagashima K, Masuda M, Matsuda M, Mochizuki N. (2004) A novel dynamin-associating molecule, formin-binding protein 17, induces tubular membrane invaginations and participates in endocytosis. *J Biol Chem* **279:** 40091–40099

Karbowski M, Jeong SY, Youle RJ (2004) Endophilin B1 is required for the maintenance of mitochondrial morphology. *J Cell Biol* **166:** 1027–1039

Kraulis PJ (1991) MOLSCRIPT: a program to produce both detailed and schematic plots of protein structure. *J Appl Crystallogr* **24:** 946–950

McMahon HT, Mills IG (2004) COP and clathrin-coated vesicle budding: different pathways, common approaches. *Curr Opin Cell Biol* **16:** 379–391

McMahon HT, Gallop JL (2005) Membrane curvature and mechanisms of dynamic cell membrane remodeling. *Nature* **438:** 590–596

Merritt EA, Bacon DJ (1997) Raster3D: photorealistic molecular graphics. *Methods Enzymol* **277:** 505–524

Modregger J, Schmidt AA, Ritter B, Huttner WB, Plomann M (2003) Characterization of Endophilin B1b, a brain-specific membrane-associated lysophosphatidic acid acyl transferase with properties distinct from endophilin A1. *J Biol Chem* **278:** 4160–4167

Nicholls A, Sharp K, Honig B (1991) Protein folding and association: insights from the interfacial and thermodynamic properties of hydrocarbons. *Proteins* **11:** 281–296

Nossal R, Zimmerberg J (2002) Endocytosis: curvature to the ENTH degree. *Curr Biol* **12:** R770–R772

Ohki T, Mikhailenko SV, Morales MF, Onishi H, Mochizuki N (2004) Transmission of force and displacement within the myosin molecule. *Biochemistry* **43:** 13707–13714

Otwinowski Z, Minor W (1997) Processing of X-ray diffraction data collected in oscillation mode. *Methods Enzymol* **276:** 307–326

Peter BJ, Kent HM, Mills IG, Vallis Y, Butler PJ, Evans PR, McMahon HT (2004) BAR domains as sensors of membrane curvature: the amphiphysin BAR structure. *Science* **303:** 495–499

Repáková J, Holopainen JM, Morrow MR, McDonald MC, Capkova P, Vattulainen I (2005) Influence of DPH on the structure and dynamics of a DPPC bilayer. *Biophys J* **88:** 3398–3410

Ringstad N, Nemoto Y, De Camilli P (1997) The SH3p4/Sh3p8/SH3p13 protein family: binding partners for synaptojanin and dynamin via a Grb2-like Src homology 3 domain. *Proc Natl Acad Sci USA* **94:** 8569–8574

Ringstad N, Nemoto Y, De Camilli P (2001) Differential expression of endophilin 1 and 2 dimers at central nervous system synapses. *J Biol Chem* **276:** 40424–40430

Roussel A, Cambillau C (1996) *TURBO-FRODO Manual*. Marseille France AFMB-CNRS, Paris, France

Sakurai A, Fukuhara S, Yamagishi A, Sako K, Kamioka Y, Masuda M, Nakaoka Y, Mochizuki N (2006) MAGI-1 is required for Rap1 activation upon cell–cell contact and for enhancement of vascular endothelial cadherin-mediated cell adhesion. *Mol Biol Cell* **17:** 966–976

Schuske KR, Richmond JE, Matthies DS, Davis WS, Runz S, Rube DA, van der Bliek AM, Jorgensen EM (2003) Endophilin is required for synaptic vesicle endocytosis by localizing synaptojanin. *Neuron* **40:** 749–762

Tarricone C, Xiao B, Justin N, Walker PA, Rittinger K, Gamblin SJ, Smerdon SJ (2001) The structural basis of Arfaptin-mediated cross-talk between Rac and Arf signalling pathways. *Nature* **411:** 215–219

Terwilliger TC (1999) Reciprocal-space solvent flattening. *Acta Crystallogr D* **55:** 1863–1871

Terwilliger TC, Berendzen J (1999) Automated MAD and MIR structure solution. *Acta Crystallogr D* **55:** 849–861

Verstreken P, Koh TW, Schulze KL, Zhai RG, Hiesinger PR, Zhou Y, Mehta SQ, Cao Y, Roos J, Bellen HJ (2003) Synaptojanin is recruited by endophilin to promote synaptic vesicle uncoating. *Neuron* **40:** 733–748

Weissenhorn W (2005) Crystal structure of the endophilin-A1 BAR domain. *J Mol Biol* **351:** 653–661

Wenk MR, De Camilli P (2004) Protein–lipid interactions and phosphoinositide metabolism in membrane traffic: insights from vesicle recycling in nerve terminals. *Proc Natl Acad Sci USA* **101:** 8262–8269

Yamagishi A, Masuda M, Ohki T, Onishi H, Mochizuki N (2004) A novel actin-bundling/filopodium-forming domain conserved in insulin receptor tyrosine kinase substrate p53 and missing in metastasis protein. *J Biol Chem* **279:** 14929–14936

Zimmerberg J, Kozlov MM (2006) How proteins produce cellular membrane curvature. *Nat Rev Mol Cell Biol* **7:** 9–19

Crystal structures of VAP1 reveal ADAMs' MDC domain architecture and its unique C-shaped scaffold

Soichi Takeda[1,2,*], Tomoko Igarashi[1], Hidezo Mori[1] and Satohiko Araki[3]

[1]Department of Cardiac Physiology, National Cardiovascular Center Research Institute, Suita, Osaka, Japan, [2]Laboratory for Structural Biochemistry, Riken Harima Institute at SPring-8, Mikazuki, Sayo, Hyogo, Japan and [3]Sugashima Marine Biological Laboratory, Graduate School of Science, Nagoya University, Toba, Mie, Japan

ADAMs (a disintegrin and metalloproteinase) are sheddases possessing extracellular metalloproteinase/disintegrin/cysteine-rich (MDC) domains. ADAMs uniquely display both proteolytic and adhesive activities on the cell surface, however, most of their physiological targets and adhesion mechanisms remain unclear. Here for the first time, we reveal the ADAMs' MDC architecture and a potential target-binding site by solving crystal structures of VAP1, a snake venom homolog of mammalian ADAMs. The D-domain protrudes from the M-domain opposing the catalytic site and constituting a C-shaped arm with cores of Ca^{2+} ions. The disintegrin-loop, supposed to interact with integrins, is packed by the C-domain and inaccessible for protein binding. Instead, the hyper-variable region (HVR) in the C-domain, which has a novel fold stabilized by the strictly conserved disulfide bridges, constitutes a potential protein–protein adhesive interface. The HVR is located at the distal end of the arm and faces toward the catalytic site. The C-shaped structure implies interplay between the ADAMs' proteolytic and adhesive domains and suggests a molecular mechanism for ADAMs' target recognition for shedding.

Introduction

ADAMs (a disintegrin and metalloproteinase) or MDC (metalloproteinase/disintegrin/cysteine-rich) proteins comprise an emerging class of mammalian metalloproteinases with potential regulatory roles in cell–cell and cell–matrix adhesion and signalling (Becherer and Blobel, 2003; Seals and Courtneidge, 2003; White, 2003; Blobel, 2005). To date, over 30 ADAMs have been identified in a variety of species from fission yeast to human. Roughly, half of these are believed to

*Corresponding author. Department of Cardiac Physiology, National Cardiovascular Center Research Institute, Fujishirodai 5-7-1, Suita, Osaka, 565-8565, Japan. Tel.: +81 6 6833 5012 ext.2381; Fax: +81 6 6872 7485; E-mail: stakeda@ri.ncvc.go.jp

function as active metalloproteinases and thus to constitute major membrane-bound sheddase that can proteolytically release cell-surface-protein ectodomains including growth factors and cytokines, their receptors and cell adhesion molecules. For example, ADAM17 (TACE, TNF-α converting enzyme) releases many cell-surface proteins including TNF-α precursor (Black et al, 1997; Moss et al, 1997) and ADAM10 (kuzbanian), which dictates lateral inhibition of Drosophila neurogenesis (Rooke et al, 1996), releases Notch ligand Delta (Qi et al, 1999) and Notch itself (Pan and Rubin, 1997). With regard to cellular interactions, fertilin α and β (ADAM1 and ADAM2, respectively) have been identified as sperm surface molecules essential for fertilization (Primakoff et al, 1987; Blobel et al, 1990, 1992) and meltrin α (ADAM12) is implicated in myogenesis (Yagami-Hiromasa et al, 1995). ADAMs have been associated with numerous diseases including arthritis, Alzheimer's disease, and cancer (Duffy et al, 2003; Moss and Bartsch, 2004). ADAM33 has been genetically linked with asthma (Van Eerdewegh et al, 2002). ADAMs uniquely display both proteolytic and adhesive activities on the cell surface, however, most of their physiological targets and the adhesion mechanisms remain unclear.

Disintegrins are small proteins (40–90 aa) isolated from snake venom typically with an Arg-Gly-Asp (RGD) recognition sequence on an extended loop (disintegrin-loop) that inhibit platelet aggregation via integrin binding (Huang et al, 1987; Calvete et al, 2005). ADAMs are unique among cell surface proteins in possessing a disintegrin (D-) domain and thus it has been suggested that integrins might be common receptors for ADAMs (Blobel et al, 1992; Evans, 2001; White, 2003). However, the RGD sequence in the ADAMs' disintegrin-loop is usually replaced by XXCD and therefore, its adhesive potential has been controversial. Both the ADAMs' D- and cysteine-rich (C-) domains are involved in the protein–protein interactions (Myles et al, 1994; Almeida et al, 1995; Zolkiewska, 1999; Iba et al, 2000; Gaultier et al, 2002; Smith et al, 2002), however, the details of the interactions have remained elusive. This is because high-resolution structures have been available only for isolated domains (Maskos et al, 1998; Orth et al, 2004; Janes et al, 2005) and no structural information has been available for the C-domain of the canonical ADAMs. To clarify the molecular mechanisms of target recognition for shedding by and of cellular adhesion via ADAMs, elucidation of the atomic structure of the ADAMs' MDC domains is indispensable.

To obtain structural data on an ADAM family member, we exploited the fact that hemorrhagic P-III snake venom metalloproteinases (SVMPs) share the ADAMs' MDC architecture (Jia et al, 1996; Evans, 2001; Fox and Serrano, 2005). Most ADAMs possess additionally, EGF-like, transmembrane and cytoplasmic domains and therefore are primarily membrane-associated, whereas SVMPs are secreted. Vascular apoptosis-inducing protein-1 (VAP1) is a disulfide-bridged

homodimer P-III SVMP isolated from *Crotalus atrox* venom (Masuda *et al*, 1998, 2000). VAP1's stability and intrinsic two-fold symmetry enabled us to solve the crystal structures at 2.5-Å resolution. The structure reveals the residues that are important for stabilizing the MDC architecture are strictly conserved throughout the primary structure among all the known ADAMs. Therefore, the present structure represents the general architecture of ADAMs' MDC domains and provides insights into the molecular mechanism of the ADAMs' target recognition.

Results

Structure determination

VAP1 yielded crystals readily, and initial phases were determined by molecular replacement method using the structure of P-I SVMP, acutolysin-C (1QUA) (Zhu *et al*, 1999) as a starting model. Although the initial model, with 99 identical residues out of 197, represented less than 50% of the total molecule, two distinct local noncrystallographic two-fold symmetry (NCS) operations (see below) allowed us to completely model the whole molecule. The native structures were determined from the crystals with two distinct space groups, $P2_12_12_1$ and $P4_12_12$, both at 2.5-Å resolution (Table I).

Orthorhombic crystals were used for inhibitor soaking and the GM6001 ((3-(*N*-hydroxycarboxamido)-2-isobutyl-propanoyl-Trp-methylamide))-bound structure was determined at 3.0-Å resolution (Table I). In either crystal forms, the asymmetric unit contained one dimer molecule. The four monomers in the two crystal forms have almost identical structures, except for slight variations in their domain orientations, terminal residues, surface loops and active-site GM6001-binding region.

MDC architecture

The MDC architecture of VAP1 is shown in Figure 1A and B. The metalloproteinase (M-) domains in the dimer are related by NCS such that their active sites point in opposite directions and an intermolecular disulfide bridge is formed between symmetry-related Cys365 residues (Figure 1A). The M-domain is followed by a disintegrin (D-) domain that is further divided into D_s- and D_a-domains (see below). The D_s-domain protrudes from the M-domain close to the Ca^{2+}-binding site I (see below) opposing the catalytic site. The D-domain forms a C-shaped arm, together with the cysteine-rich (C-) domain, with its concave surface toward the M-domain. There are no direct interactions between the arm and the M-domain. Notably, the distal portion of the C-domain comes close to

Table I Data collection and refinement statistics

	Native (orthorhombic)	Native (tetragonal)	GM6001-bound
Data collection			
Space group	$P2_12_12_1$	$P4_12_12$	$P2_12_12_1$
Cell dimensions			
a, b, c (Å)	86.7, 93.3, 137.7	93.9,93.9,244.8	86.3, 91.4, 136.0
α, β, γ (deg)	90, 90, 90	90, 90, 90	90, 90, 90
Resolution (Å)	50–2.50 (2.59–2.50)	50–2.50 (2.59–2.50)	50–2.95 (3.06–2.95)
R_{merge}[a]	0.072 (0.369)	0.084 (0.380)	0.072 (0.367)
$I/\sigma I$	14.4 (2.9)	18.7 (7.1)	12.6 (4.3)
Completeness (%)	99.4 (98.8)	99.7 (99.6)	99.9 (99.4)
Redundancy	3.91	12.7	4.95
Refinement			
Resolution (Å)	50–2.50 (2.59–2.50)	50–2.50 (2.59–2.50)	50–2.95 (3.06–2.95)
No. of reflections	38874	38786	23295
R_{work}[b]$/R_{free}$[c]	0.212/0.258	0.229/0.269	0.208/0.264
No. of atoms			
Protein	6558	6513	6558
Zn^{2+}	2	2	2
Ca^{2+}	4	4	4
Co^{3+}	1		1
N-acetyl glucosamine	56	42	56
GM6001			56
Water	205	165	35
B-factors			
Protein	44.9	51.2	55.4
Zn^{2+}	40.9	41.6	46.4
Ca^{2+}	43.5	52.4	49.3
Co^{3+}	35.5		56.8
N-acetyl glucosamine	69.8	65.1	75.8
GM6001			78.6
Water	39.8	41.5	37.0
R.m.s deviations			
Bond lengths (Å)	0.0052	0.0080	0.0038
Bond angles (deg)	1.18	1.39	0.92

[a]$R_{merge} = \sum_{hkl}\sum_i|I_i(hkl)-\langle I(hlk)\rangle| / \sum_{hkl}\sum_i I_i(hkl)$, where $I_i(hkl)$ is the *i*th intensity measurement of reflection *hkl* and $\langle I(hlk)\rangle$ is its average.
[b]$R_{work} = \sum(||F_{obs}|-|F_{calc}||/\sum|F_{obs}|$.
[c]R_{free} = R-value for a randomly selected subset (5%) of the data that were not used for minimization of the crystallographic residual.
Highest resolution shell is shown in parenthesis.
For each data set, single crystal was used for measurement.
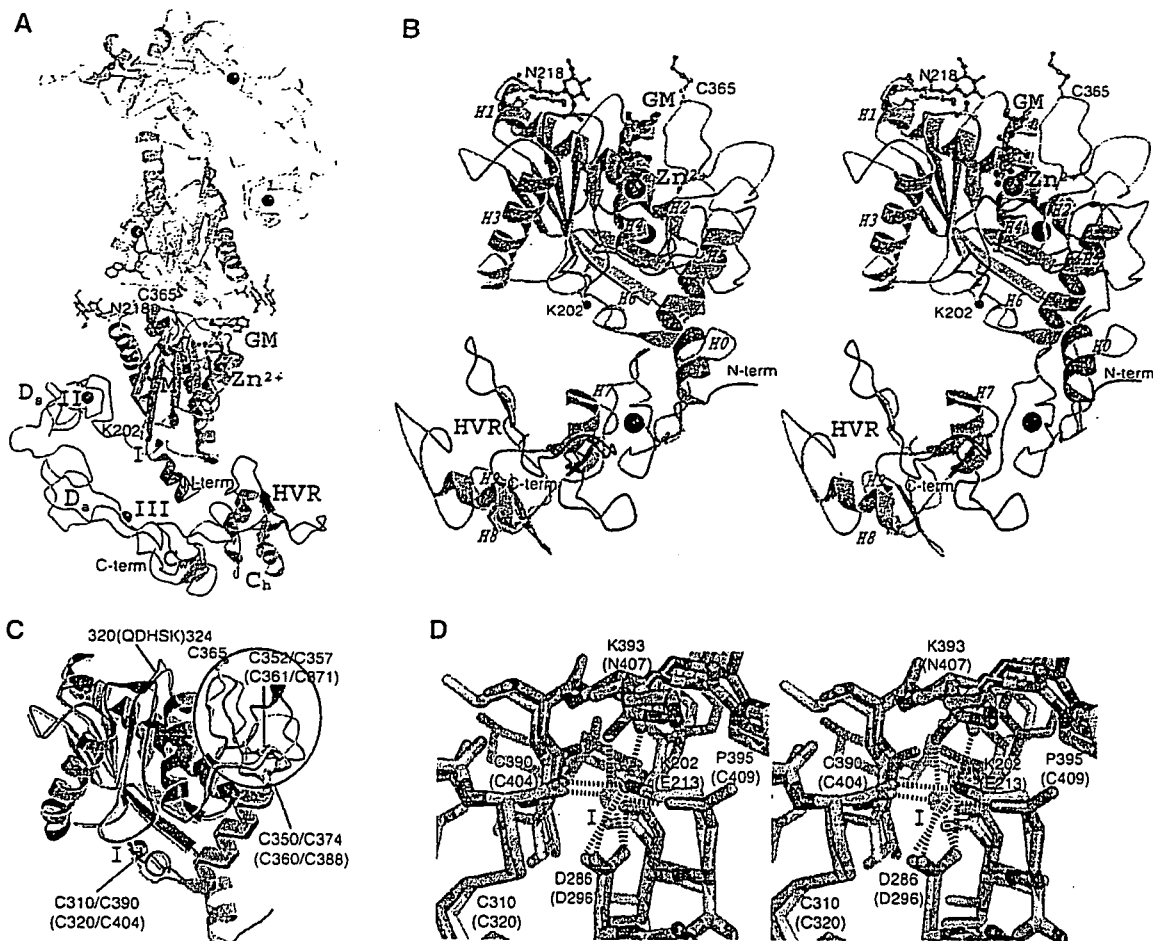
Figure 1 MDC architecture. (A) VAP1 dimer viewed from the NCS axis. The H0-helix, M-domain, linker, D_s-, D_a-, C_w-, and C_h-domains and HVRs belonging to the one monomer are shown in red, yellow, gray, cyan, pink, gray, green and blue, respectively. The disulfide-linked counterpart is shown in gray. Zinc and calcium ions are represented as red and black spheres, respectively. The NAG (N-acetyl-glucosamine, in orange) moieties linked to Asn218, the calcium-mimetic Lys202 and the bound inhibitor GM6001 (GM, in green) are in ball-stick representations. (B) Stereo view of VAP1 monomer from the direction nearly perpendicular to (A). The helix numbers are labelled. (C) Superposition of the M-domains of ADAM33 (blue) and VAP1 (yellow). The calcium ion bound to site I and the zinc ion in ADAM33 are represented by black and red spheres, respectively. The disulfide bridges are indicated in black and blue letters for VAP1 and ADAM33, respectively. The QDHSK sequence for the dimer interface in VAP1 (residues 320–324) is in red. (D) Comparison of the calcium-binding site I structures of ADAM33 (blue) and VAP1 (yellow) in stereo. The residues in ADAM33 and in VAP1 are labelled in blue and black, respectively. A calcium ion and a water molecule bound to ADAM33 are represented as green and red spheres, respectively. The ammonium group of Lys202 in VAP1 occupies the position of the calcium ion in ADAM33. In ADAM33 (Orth et al, 2004), side-chain oxygen atoms of Glu213, Asp296 and Asn407, the carbonyl oxygen of Cys404 and a water molecule form the corners of a pentagonal bipyramid and ligand to the calcium ion.

and faces toward the catalytic site in the M-domain. The C-terminus Tyr610 is located proximal to the boundary between the D_a- and C-domains (Figure 1A and B). Aside from Cys365, each monomer contains 34 cysteinyl residues, all of which are involved in disulfide bonding, and their spacings are strictly conserved among ADAMs (Figure 2 and Supplementary Figure 1) except within the substrate-binding (between the helices H4 and H5) and the HVR (see below) regions. Figure 2 provides a selected subset of the sequence alignments and the entire alignments of VAP1 and 39 ADAM sequences, including all 23 human ADAMs so far available, can be found as Supplementary Figure 1.

M-domain

Each VAP1 M-domain corresponds to a very similar structure to that of ADAM33 (Orth et al, 2004), with a flat ellipsoidal shape having a central core made up of five stranded β-sheets and five α-helices and a conserved methionine (Met-turn)

below the active site histidine residues, which bears the typical structural feature of metzincin family of metallopro-teinases (Bode et al, 1993). However, they differ in the dimer interface and the loop structure around the substrate-binding site (Figure 1C) that corresponds to the variable region in the primary structure (between the helices H4 and H5, see Figure 2). The N-terminal helix (H0) is also unique in VAP1. The dimer interface is best characterized by the recognition sequence QDHSK (residues 320–324, see Figure 1C and Supplementary Figure 2A–C) and by Cys365, however these are not conserved among ADAMs; therefore, none of the ADAMs' M-domains are suggested to form a stable dimer as VAP1. A peptide-like hydroxamate inhibitor GM6001 binds to VAP1 (Figure 1A and B, and Supplementary Figure 2D and E) in exactly the same manner as in the marimastat-ADAM33 M-domain complex (Orth et al, 2004), suggesting that the catalytic sites of VAP1 and ADAM33 share a common substrate recognition mechanism. The ADAM33
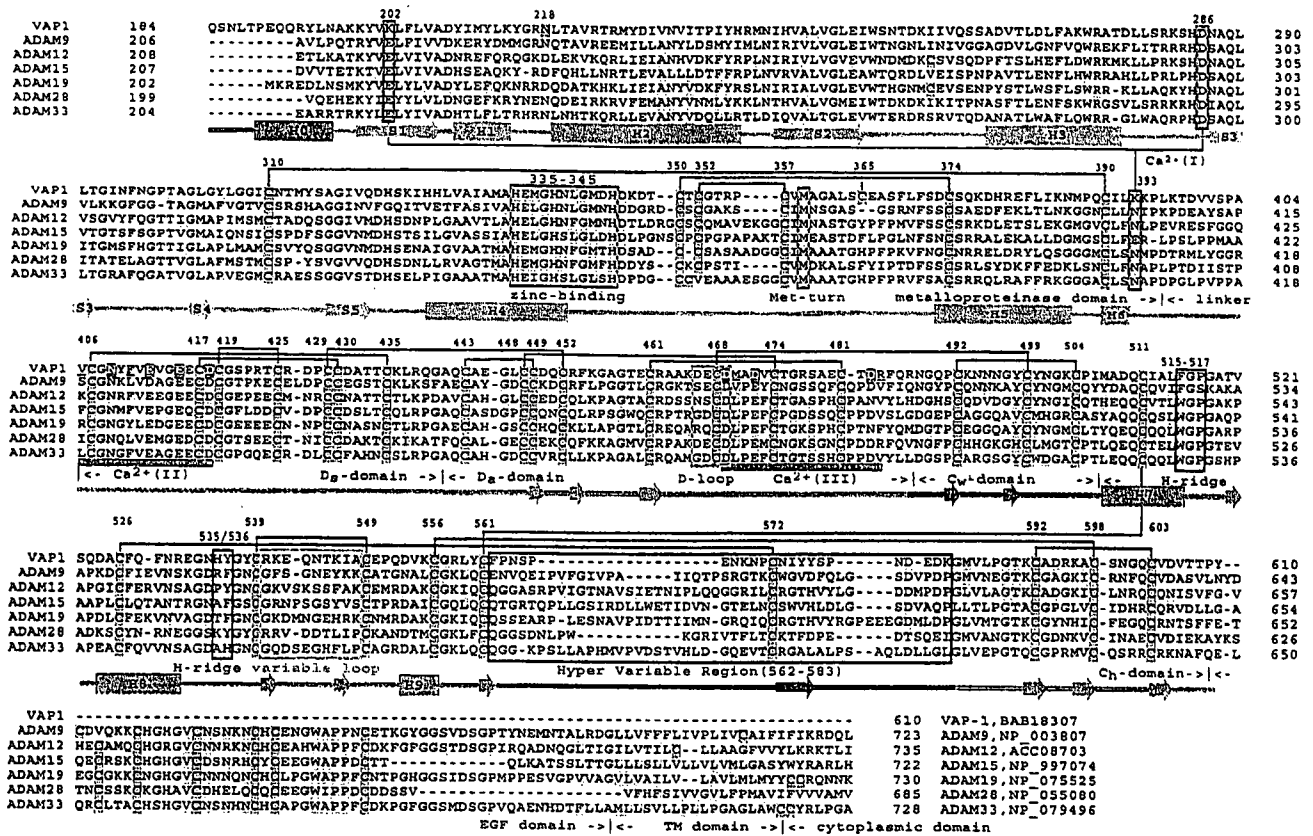
-431-

Figure 2 Sequence alignments of VAP1 and human ADAMs. The cysteinyl residues and the conserved residues are shaded in pink and yellow, respectively. Disulfide bridges, secondary structures and domains are drawn schematically. The HVR, calcium-binding site I, catalytic site and disintegrin-loop (D-loop) are boxed in blue, red, green and cyan, respectively. The hydrophobic ridges (H-ridges) are indicated. Calcium-binding sites II and III and the coordinating residues (shaded in red) are indicated. The NCBI accession numbers for the sequences are indicated.

M-domain structure suggests that most ADAMs have a Ca^{2+}-binding site (designated Ca^{2+}-binding site I) opposing the active-site cleft; however, in VAP1, the distal ammonium group of Lys202 substitutes for the Ca^{2+} ion (Figure 1D). Replacement of the calcium-coordinating glutamate residue with lysine also occurs in ADAM16, ADAM25 and ADAMs38–40 (Supplementary Figure 1).

C-shaped arm

The D-domain follows the M-domain, with a short linker that allows slightly variable domain orientations at V405 as a pivotal point (Figure 3C). The D-domain is further divided into two structural subdomains (Figure 3), the 'shoulder' (D_s-domain, residues 396–440) and the 'arm' (D_a-domain, residues 441–487). The D_s- and D_a-domains constitute a continuous C-shaped arm, together with the following N-terminus region of the C-domain which we designate the 'wrist' (C_w-domain, residues 488–505). There are three disulfide bonds in the D_s-domain, three in the D_a-domain and one in the C_w-domain. The subdomains are connected by single disulfide bridges (Figures 2 and 3A) with slightly variable angles (Figure 3B).

Both the D_s- and D_a-domains contain structural calcium-binding sites. In the D_s-domain, the side-chain oxygen atoms in residues Asn408, Glu412, Glu415 and Asp418, and the carbonyl oxygen atoms of Val405 and Phe410 are involved in pentagonal bipyramidal coordination and constitute Ca^{2+}-binding site II (Figures 2 and 3A). Notably, these residues are

strictly conserved among all known ADAMs (Supplementary Figure 1). However, the side-chain oxygens of Asp469, Asp472 and Asp483, and carbonyl oxygens of Met470 and Arg484 form the corners of a pentagonal bipyramid to the calcium ligand and constitute the D_a-domain Ca^{2+}-binding site III (Figures 2 and 3A) and these residues are highly conserved among ADAMs except ADAM10 and ADAM17 (Supplementary Figure 1). Because of the few secondary-structural elements, bound calcium ions and the disulfide bridges are essential for the structural rigidity of ADAM's C-shaped arm. The RGD-containing disintegrin trimestatin (Fujii *et al*, 2003) has a similar structure with the D_a-domain (r.m.s.d of 1.24 Å, Figure 3B); however, no disintegrins have been shown to bind Ca^{2+} ions.

Using isolated D-domains or portions thereof, numerous ADAMs and P-III SVMPs have been shown to interact specifically with particular integrins (Evans, 2001; White, 2003; Calvete *et al*, 2005). However, the disintegrin-loop is packed against the C_w-domain and a disulfide bridge (Cys468–Cys499) further stabilizes the continuous structure (Figure 3A). Therefore, the disintegrin-loop is inaccessible for protein binding.

Hand domain

The 'hand' domain (C_h-domain, residues 505–610) follows the C_w-domain. The C_h-domain, together with the C_w-domain, constitutes a novel fold (Figure 4A). In either crystal form, VAP1 dimers interact with molecules of neighboring

A

B

C
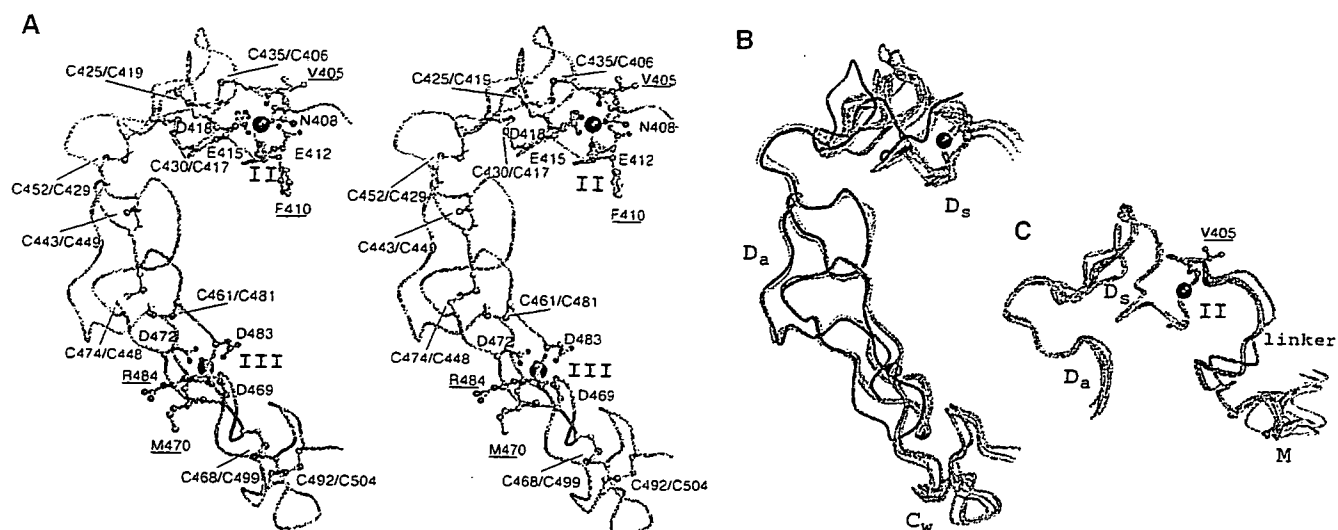
Figure 3 Arm structure. (A) Arm structure *in stereo*. The D_s-, D_a-, and C_w-domains are in cyan, pink and light green, respectively. The calcium-coordinating residues and the disulfide bridges are shown in red and green, respectively. The residues with carbonyl oxygen atoms involved in calcium coordination are underlined. Calcium ions are represented as black spheres. The disintegrin-loop (DECD) is in blue. (B) Superimposition of the four D_a-domains of VAP1 and trimestatin (1J2L). Trimestatin and its RGD loop are shown in red and blue, respectively. (C) Superimposition of the four D_s-domains. The linker between the M- and D_s-domains is shown in gray. Val405 at the pivotal point is indicated.

A

B

C

D
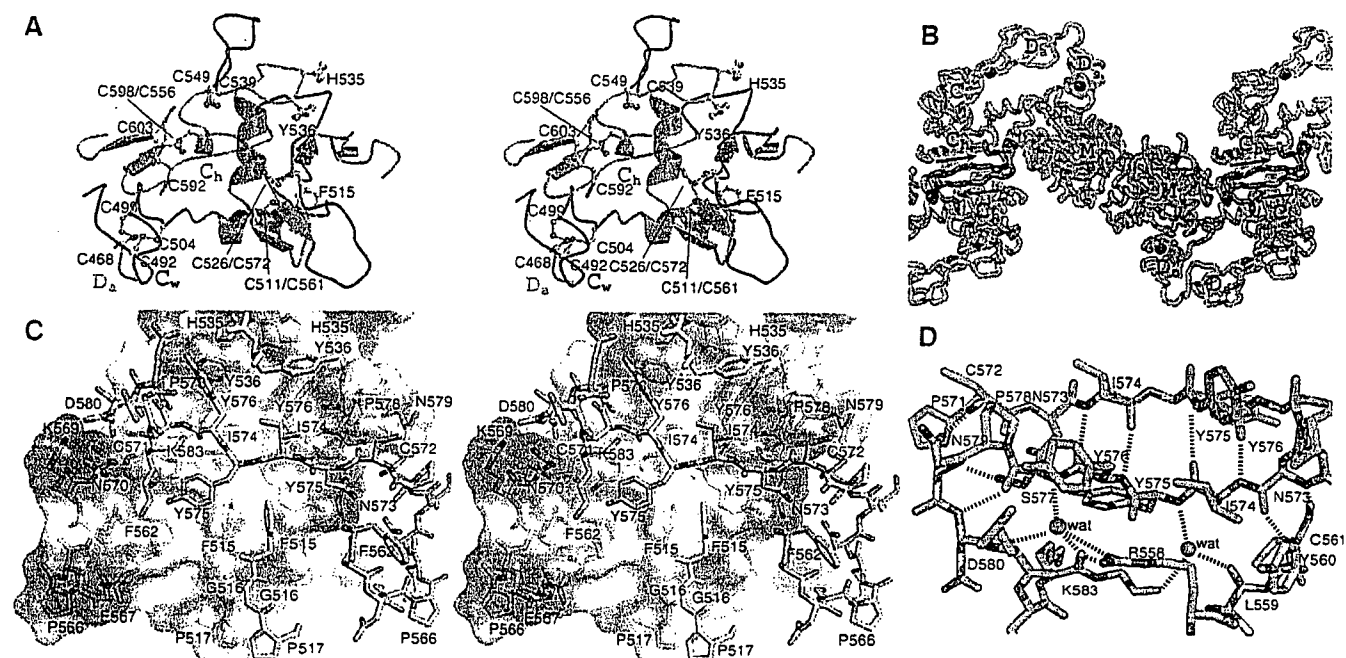
Figure 4 C-domain architecture and HVR. (A) The C-domain architecture *in stereo*. The C_w- and C_h-domains are in gray and light green, respectively. The disulfide bridges and the residues forming the hydrophobic ridges are indicated. The HVR and its NCS counterpart are shown in red and blue, respectively. The variable loop (residues 539–549), flanked by two adjacent cysteine residues, is in green. (B) Crystal packing in the orthorhombic crystal. The crystallographically equivalent molecules (HVRs) are in cyan (blue) and pink (red), respectively. The arrows indicate the directions of the HVR chains. Zinc and calcium ions are represented as red and black spheres, respectively. (C) Interactions between the HVRs (cyan and pink) *in stereo*. The molecular surface of the cyan molecule is shown with the electrochemical surface potential (red to blue). The residues constituting the hydrophobic ridges are in yellow. The residues are labelled in blue and red for cyan and pink, respectively. (D) Water-mediated hydrogen-bond network in the HVR. The HVR residues are in pink and cyan; non-HVR residues in the pink molecule are in gray.

units through the C_h-domains such that the molecules form a handshake (Figure 4B). Each C_h-domain interacts with its counterpart through a relatively large complementary surface of 860 Å^2 forming another NCS at the center, although VAP1 exists as dimers, not as oligomers, and is mono-dispersed in solution (data not shown).

HVR as a potential adhesive interface

C_h-domain residues 562–583 are predominantly involved in the handshake (Figure 4B). This is the region in which the ADAM sequences are most divergent and variable in length (16–55 aa) (Figure 2 and Supplementary Figure 1). We have designated this as the hyper-variable region (HVR). The HVR

-433-

is subdivided into two structural elements. The N-terminal portion (residues 562–572) fits into an extended loop, filling the gap between the M-domain and the neighboring molecule's C_h-domain and thus fixing the position of the arm (Figure 4B). The variable structures and less-specific interactions suggest that this loop is stabilized by crystal packing. Some ADAMs possess a putative fusion peptide in this segment typical of viral fusion proteins (Blobel *et al*, 1992; Yagami-Hiromasa *et al*, 1995), although their role in the actual fusion process has not been demonstrated. However, the remainder of the HVR (residues 572–583) interacts extensively with its counterpart by forming an antiparallel β strand at the center (Figure 4C and D). Although the ability to form β strand is predictable from the sequence, this β strand is stabilized mainly by interchain interactions (Figure 4D). There are no intrachain hydrogen bonds between residues 574–577 and the remainder of the C_h-domain; however a water-mediated hydrogen-bond network stabilizes this segment (Figure 4D). Therefore, it appears, that this β strand might be formed by the induced-fit mechanism upon the association of the C_h-domains and that the conserved disulfide bond (Cys526–Cys572, see Figure 4D) may stabilize the structure when the HVRs are isolated in solution. In addition to the main-chain hydrogen bonds, side-chain atoms (particularly residues I574, Y575, Y576 and P578) in the HVR β strand contribute numerous von der Waals interactions with their counterparts. Aside from the HVR, aromatic residues located at both sides of the β strand in close proximity to the NCS axis create additional interaction surfaces: residues Phe515, Gly516, His535 and Tyr536 in the loop regions form hydrophobic ridges that fit complementarily into the NCS region (Figure 4C). The hydrophobic ridges are highly conserved among ADAMs (Figure 2 and Supplementary Figure 1), thus, in part, they may also constitute binding surfaces.

Discussion

The VAP1 structures reveal highly conserved structural calcium-binding sites and the numbers and the spacings of cysteinyl residues that are essential for maintaining structural rigidity and spatial arrangement of the ADAMs' MDC domains. The C-shaped MDC architecture implies meaningful interplay between the domains and their potential roles in physiological functions.

The HVR creates a novel interaction interface in collaboration with the conserved hydrophobic ridges. Different ADAMs have distinct HVR sequences, which result in distinct surface features, thus, they may function in specifying binding proteins. The HVR is at the distal end of the C-shaped arm and points toward the M-domain catalytic site, with a distance of ~4 nm in between them. Collectively, these observations suggest that the HVR captures the target or associated protein that is processed by the catalytic site (Figure 5). The disintegrin portion is located opposit to and apart from the catalytic site and, thus, might play a primary role as a scaffold that allocates these two functional units spatially. The C-shaped structure also implies how the ADAMs' C-domains cooperate with their M-domains (Reddy *et al*, 2000; Smith *et al*, 2002). In membrane-bound ADAMs, the EGF-like domain (~60 aa) follows the C_h-domain (Figure 2) and presumably works as a rigid spacer connecting the MDC-domains with and orientating against the membrane-span-
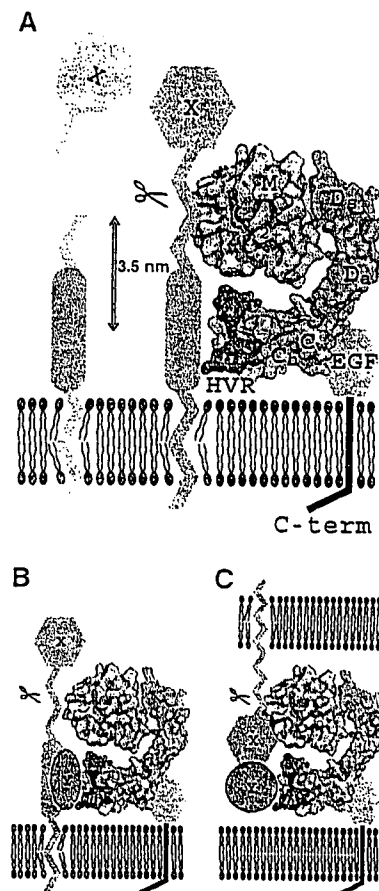
Figure 5 Models for ADAM's shedding. The molecular surface of the VAP1 monomer, without VAP1's unique H0-helix, are colored as in Figure 1A. Hydrophobic ridges are in yellow. EGF-like, transmembrane and cytoplasmic domains are represented schematically. (A) Membrane-anchored substrate molecule 'X' is directly recognized and captured by the HVR on the membrane-bound ADAM molecule. The distance between the center of the HVR (Tyr575) and the catalytic zinc ion is about 3.5 nm. (B) Substrate 'X' is recognized by the ADAM HVR via binding with an associated protein 'Y'. (C) ADAM cleaves substrate 'X' in *trans* via binding with an associated protein 'Y'.

ning region (Figure 5A). Many ADAMs are proteolytically inactive (because of the defects in the catalytic HEXXHXXGXXHD sequence or the post-translational removal of the M-domain), and several of these are important developmentally. Therefore, the HVR may also work to modulate cell–cell and cell–matrix interactions. There is some experimental evidence for C-domain-mediated adhesion. Peptides encompassing the HVR and the hydrophobic ridge from P-III SVMPs interfere with platelet interaction and collagen binding (Kamiguti *et al*, 2003). A recombinant atrolysin-A C-domain specifically binds collagen I and von Willebrand factor (vWF) and blocks collagen–vWF interaction (Jia *et al*, 2000; Serrano *et al*, 2005). ADAM12 interacts with cell-surface syndecan through its C-domain and mediates integrin-dependent cell spreading (Iba *et al*, 2000). The D/C-domain portion of ADAM13 binds to the ECM proteins laminin and fibronectin (Gaultier *et al*, 2002). However, most of these studies do not assign specific regions of the C-domain to these interactions and the molecular recognition mechanisms are to be elucidated.

ADAM10 and ADAM17 lack the Ca^{2+}-binding site III and show less sequence similarities in the C-domain with other

-434-

canonical ADAMs (Supplementary Figure 1). Comparison of the recently solved ADAM10 D/C-domain partial structure (ADAM10$_{D+C}$) (Janes et al, 2005) and that of VAP1 reveals that the atypical ADAM10 shares the continuous D$_a$/C$_w$ structure and the C$_h$-domain scaffold with VAP1; however, it has an disordered D$_s$-domain and an alternate HVR structure and a different orientation between C$_w$- and C$_h$-domains (Figure 6). The locations of four of the five disulfide bridges within the C$_h$-domain are conserved between VAP1 and ADAM10 (Figure 6B and C) and thus, they enabled us to align the two sequences (Figure 6E). Based on this alignment, we completed entire alignments (Supplementary Figure 1) including 38 sequences of mammalian ADAMs and Schizosaccharomyces pombe Mde10 (Nakamura et al, 2004), presumably the founding member of the ADAM family in evolutionary terms. The ADAM10$_{D+C}$ structure lacks the eight residues (583–590 in ADAM10) that may form a flexible loop. However, VAP1 (Figure 6E) and the canonical ADAMs except for ADAM8 (Supplementary Figure 1) have extra 16 residues in this segment that, in part, forms a variable loop, flanked by the adjacent cysteinyl residues (Cys539 and Cys549 in VAP1) and protrudes from the main body of the C-domain (Figures 4A and 6B). The variable loop has highest temperature factor in the molecule and resembles to the

disintegrin-loop, thus can be an additional protein-binding interface. The six VAP1 monomer molecules represent almost the same C$_w$/C$_h$ domain orientation (data not shown), however that is distinct from that of ADAM10 (Figure 5A). Thus, the possibility whether different ADAMs have distinct C$_w$/C$_h$ domain orientation remains to be established. Janes et al (2005) have shown that the three glutamate residues outside of HVR are essential for ADAM10-mediated ephrin proteolysis in trans, however, roles of the ADAM10 HVR has not been examined. An extensive molecular surface of the elongated arm structure (12 000 Å^2 for the VAP1 D/C-domains) might reveal additional protein–protein interaction interfaces other than the HVR. Multiple charged residues in the D-domain are essential for ADAM28 binding to α4β1 (Bridges et al, 2003) and the RX$_6$DLPEF motif has been proposed for integrin α9β1 binding (Eto et al, 2002). However, the D-domain portion of the C-shaped scaffold is away from the catalytic site; thus, those additional sites might not directly serve as target recognition interfaces for catalysis.

Uniquely among cell-surface proteins, ADAMs display both proteolytic and adhesive activities. The VAP1 structure reveals that these functions are spatially allocated to the ends of the unique C-shaped scaffold and face each other. This spatial allocation of the functional sites provide us insights
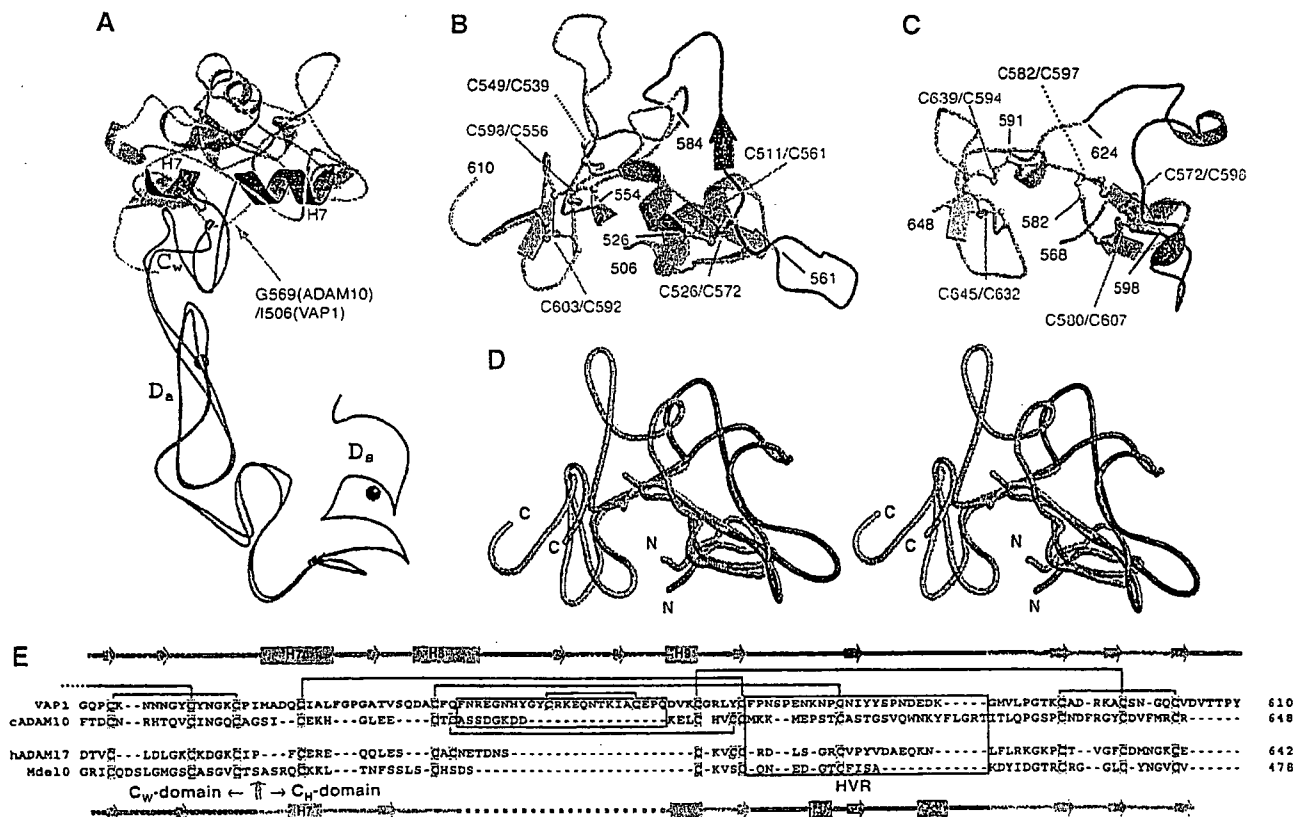

Figure 6 Comparison of the VAP1 and ADAM10 D/C domains. (A) Superimposition of the D$_a$-domains of ADAM10 and VAP1. The D$_s$/D$_a$/C$_w$-domains and the H7 helix of VAP1 and those of ADAM10 are shown in blue and red, respectively. The C$_h$-domains of VAP1 and ADAM10 are shown in cyan and pink, respectively. The arrow indicates the pivotal point between the C$_w$- and C$_h$-domains. Bound Ca^{2+} ions in VAP1 are shown as black spheres. (B) Ribbon representation of the C$_h$-domain of VAP1. The HVR is shown in blue. The common scaffold between the VAP1 and ADAM10 C$_h$-domains are shown in cyan and the segment lacking in ADAM10 is shown in light green. Disulfide bridges are indicated. (C) Ribbon representation of the C$_h$-domain of ADAM10. The HVR is shown in red. Disulfide brides are indicated. (D) Superimposition of the C$_h$-domains of VAP1 and ADAM10 in stereo with the colors as in (B, C). The N- and C-termini of the C$_h$-domains are indicated. (E) Structure-based alignments of VAP1, bovine ADAM10 (cADAM10), human ADAM17 (hADAM17) and S. pombe Mde10 (Mde10) C$_w$/C$_h$-domains. Secondary structures and the disulfide bridges are represented schematically. The HVR sequences and the missing segment in the ADAM10 structure are boxed in blue and green, respectively.

-435-

topologies and should be grouped into a common family, the 'metzincins'. *FEBS Lett* **331**: 134–140

Bridges LC, Hanson KR, Tani PH, Mather T, Bowditch RD (2003) Integrin alpha4beta1-dependent adhesion to ADAM 28 (MDC-L) requires an extended surface of the disintegrin domain. *Biochemistry* **42**: 3734–3741

Brunger AT, Adams PD, Clore GM, DeLano WL, Gros P, Grosse-Kunstleve RW, Jiang JS, Kuszewski J, Nilges M, Pannu NS, Read RJ, Rice LM, Simonson T, Warren GL (1998) Crystallography & NMR system: a new software suite for macromolecular structure determination. *Acta Crystallogr D* **54** (Part 5): 905–921

Calvete JJ, Marcinkiewicz C, Monleon D, Esteve V, Celda B, Juarez P, Sanz L (2005) Snake venom disintegrins: evolution of structure and function. *Toxicon* **45**: 1063–1074

CCP4 (1994) The CCP4 suite: programs for protein crystallography. *Acta Crystallogr D* **50**: 760–763

Duffy MJ, Lynn DJ, Lloyd AT, O'Shea CM (2003) The ADAMs family of proteins: from basic studies to potential clinical applications. *Thromb Haemost* **89**: 622–631

Eto K, Huet C, Tarui T, Kupriyanov S, Liu HZ, Puzon-McLaughlin W, Zhang XP, Sheppard D, Engvall E, Takada Y (2002) Functional classification of ADAMs based on a conserved motif for binding to integrin alpha 9beta 1: implications for sperm-egg binding and other cell interactions. *J Biol Chem* **277**: 17804–17810

Evans JP (2001) Fertilin beta and other ADAMs as integrin ligands: insights into cell adhesion and fertilization. *BioEssays* **23**: 628–639

Fox JW, Serrano SM (2005) Structural considerations of the snake venom metalloproteinases, key members of the M12 reprolysin family of metalloproteinases. *Toxicon* **45**: 969–985

Fujii Y, Okuda D, Fujimoto Z, Horii K, Morita T, Mizuno H (2003) Crystal structure of trimestatin, a disintegrin containing a cell adhesion recognition motif RGD. *J Mol Biol* **332**: 1115–1122

Gaultier A, Cousin H, Darribere T, Alfandari D (2002) ADAM13 disintegrin and cysteine-rich domains bind to the second heparin-binding domain of fibronectin. *J Biol Chem* **277**: 23336–23344

Huang TF, Holt JC, Lukasiewicz H, Niewiarowski S (1987) Trigramin. A low molecular weight peptide inhibiting fibrinogen interaction with platelet receptors expressed on glycoprotein IIb–IIIa complex. *J Biol Chem* **262**: 16157–16163

Iba K, Albrechtsen R, Gilpin B, Frohlich C, Loechel F, Zolkiewska A, Ishiguro K, Kojima T, Liu W, Langford JK, Sanderson RD, Brakebusch C, Fassler R, Wewer UM (2000) The cysteine-rich domain of human ADAM 12 supports cell adhesion through syndecans and triggers signaling events that lead to beta1 integrin-dependent cell spreading. *J Cell Biol* **149**: 1143–1156

Janes PW, Saha N, Barton WA, Kolev MV, Wimmer-Kleikamp SH, Nievergall E, Blobel CP, Himanen JP, Lackmann M, Nikolov DB (2005) Adam meets Eph: an ADAM substrate recognition module acts as a molecular SWITCH for Ephrin cleavage *in trans. Cell* **123**: 291–304

Jia LG, Shimokawa K, Bjarnason JB, Fox JW (1996) Snake venom metalloproteinases: structure, function and relationship to the ADAMs family of proteins. *Toxicon* **34**: 1269–1276

Jia LG, Wang XM, Shannon JD, Bjarnason JB, Fox JW (2000) Inhibition of platelet aggregation by the recombinant cysteine-rich domain of the hemorrhagic snake venom metalloproteinase, atrolysin A. *Arch Biochem Biophys* **373**: 281–286

Kamiguti AS, Gallagher P, Marcinkiewicz C, Theakston RD, Zuzel M, Fox JW (2003) Identification of sites in the cysteine-rich domain of the class P-III snake venom metalloproteinases responsible for inhibition of platelet function. *FEBS Lett* **549**: 129–134

Maskos K, Fernandez-Catalan C, Huber R, Bourenkov GP, Bartunik H, Ellestad GA, Reddy P, Wolfson MF, Rauch CT, Castner BJ, Davis R, Clarke HR, Petersen M, Fitzner JN, Cerretti DP, March CJ, Paxton RJ, Black RA, Bode W (1998) Crystal structure of the catalytic domain of human tumor necrosis factor-alpha-converting enzyme. *Proc Natl Acad Sci USA* **95**: 3408–3412

Masuda S, Hayashi H, Araki S (1998) Two vascular apoptosis-inducing proteins from snake venom are members of the metalloprotease/disintegrin family. *Eur J Biochem* **253**: 36–41

Masuda S, Ohta T, Kaji K, Fox JW, Hayashi H, Araki S (2000) cDNA cloning and characterization of vascular apoptosis-inducing protein 1. *Biochem Biophys Res Commun* **278**: 197–204

Moss ML, Bartsch JW (2004) Therapeutic benefits from targeting of ADAM family members. *Biochemistry* **43**: 7227–7235

Moss ML, Jin SL, Milla ME, Bickett DM, Burkhart W, Carter HL, Chen WJ, Clay WC, Didsbury JR, Hassler D, Hoffman CR, Kost TA, Lambert MH, Leesnitzer MA, McCauley P, McGeehan G, Mitchell J, Moyer M, Pahel G, Rocque W, Overton LK, Schoenen F, Seaton T, Su JL, Warner J, Willard D, Becherer JD (1997) Cloning of a disintegrin metalloproteinase that processes precursor tumour-necrosis factor-alpha. *Nature* **385**: 733–736

Myles DG, Kimmel LH, Blobel CP, White JM, Primakoff P (1994) Identification of a binding site in the disintegrin domain of fertilin required for sperm-egg fusion. *Proc Natl Acad Sci USA* **91**: 4195–4198

Nakamura T, Abe H, Hirata A, Shimoda C (2004) ADAM family protein Mde10 is essential for development of spore envelopes in the fission yeast *Schizosaccharomyces pombe. Eukaryot Cell* **3**: 27–39

Orth P, Reichert P, Wang W, Prosise WW, Yarosh-Tomaine T, Hammond G, Ingram RN, Xiao L, Mirza UA, Zou J, Strickland C, Taremi SS, Le HV, Madison V (2004) Crystal structure of the catalytic domain of human ADAM33. *J Mol Biol* **335**: 129–137

Pan D, Rubin GM (1997) Kuzbanian controls proteolytic processing of Notch and mediates lateral inhibition during *Drosophila* and vertebrate neurogenesis. *Cell* **90**: 271–280

Perrakis A, Morris R, Lamzin VS (1999) Automated protein model building combined with iterative structure refinement. *Nat Struct Biol* **6**: 458–463

Primakoff P, Hyatt H, Tredick-Kline J (1987) Identification and purification of a sperm surface protein with a potential role in sperm-egg membrane fusion. *J Cell Biol* **104**: 141–149

Qi H, Rand MD, Wu X, Sestan N, Wang W, Rakic P, Xu T, Artavanis-Tsakonas S (1999) Processing of the notch ligand delta by the metalloprotease Kuzbanian. *Science* **283**: 91–94

Reddy P, Slack JL, Davis R, Cerretti DP, Kozlosky CJ, Blanton RA, Shows D, Peschon JJ, Black RA (2000) Functional analysis of the domain structure of tumor necrosis factor-alpha converting enzyme. *J Biol Chem* **275**: 14608–14614

Rooke J, Pan D, Xu T, Rubin GM (1996) KUZ, a conserved metalloprotease-disintegrin protein with two roles in *Drosophila* neurogenesis. *Science* **273**: 1227–1231

Seals DF, Courtneidge SA (2003) The ADAMs family of metalloproteases: multidomain proteins with multiple functions. *Genes Dev* **17**: 7–30

Serrano SM, Jia LG, Wang D, Shannon JD, Fox JW (2005) Function of the cysteine-rich domain of the haemorrhagic metalloproteinase atrolysin A: targeting adhesion proteins collagen I and von Willebrand factor. *Biochem J* **391**: 69–76

Smith KM, Gaultier A, Cousin H, Alfandari D, White JM, DeSimone DW (2002) The cysteine-rich domain regulates ADAM protease function *in vivo. J Cell Biol* **159**: 893–902

Van Eerdewegh P, Little RD, Dupuis J, Del Mastro RG, Falls K, Simon J, Torrey D, Pandit S, McKenny J, Braunschweiger K, Walsh A, Liu Z, Hayward B, Folz C, Manning SP, Bawa A, Saracino L, Thackston M, Benchekroun Y, Capparell N, Wang M, Adair R, Feng Y, Dubois J, FitzGerald MG, Huang H, Gibson R, Allen KM, Pedan A, Danzig MR, Umland SP, Egan RW, Cuss FM, Rorke S, Clough JB, Holloway JW, Holgate ST, Keith TP (2002) Association of the ADAM33 gene with asthma and bronchial hyperresponsiveness. *Nature* **418**: 426–430

White JM (2003) ADAMs: modulators of cell–cell and cell–matrix interactions. *Curr Opin Cell Biol* **15**: 598–606

Yagami-Hiromasa T, Sato T, Kurisaki T, Kamijo K, Nabeshima Y, Fujisawa-Sehara A (1995) A metalloprotease-disintegrin participating in myoblast fusion. *Nature* **377**: 652–656

Zhu X, Teng M, Niu L (1999) Structure of acutolysin-C, a haemorrhagic toxin from the venom of Agkistrodon acutus, providing further evidence for the mechanism of the pH-dependent proteolytic reaction of zinc metalloproteinases. *Acta Crystallogr D* **55**: 1834–1841

Zolkiewska A (1999) Disintegrin-like/cysteine-rich region of ADAM 12 is an active cell adhesion domain. *Exp Cell Res* **252**: 423–431

-436-

into the molecular mechanism of ADAMs' target recognition, which ADAMs shed which key substrates in specific biological events. Since ADAMs are potential therapeutic targets, the distinct surface feature created by the HVR of the individual ADAMs might also provide insights into the future design of drugs with higher specificity for each member of ADAMs. We suggest that the HVR, not the disintegrin domain, should be the focus of searches for physiological targets of ADAMs.

Materials and methods

Protein preparation and crystallization

The details of the preparation, crystallization and preliminary X-ray analysis of VAP1 will be described elsewhere (T Igarashi et al, in preparation). VAP1 was isolated from the crude snake Crotalus atrox venom (Sigma-Aldrich, USA) and subjected to sitting- or hanging-drop vapor diffusion crystallization. Two distinct crystal forms ($P2_12_12_1$ and $P4_12_12$) were obtained with the reservoir solution containing 15% polyethyleneglycol 8000 and 100 mM sodium cacodylate at pH 6.5, with (orthorhombic form) or without (tetragonal form) 20 mM cobaltous chloride hexahydrate. GM6001-bound crystals were prepared by adding GM6001 (CALBIOCHEM) to the drop with the orthorhombic crystal at a final concentration qof 0.33 mM (twice the protein concentration) followed by a 12-h incubation. Crystals were flash-frozen under the nitrogen flow at 90 K.

Diffraction data collection

All the diffraction data were collected at SPring-8 beamlines using either ADSC quantum 310R CCD (for the inhibitor-bound crystal at the beamline BL41XU with $\lambda = 1$ Å), Rigaku R-axis V imaging plate (for orthorhombic native crystal at the beamline BL45PX with $\lambda = 1$ Å) or Jupitor CCD (for the tetragonal crystal at the beamline BL45PX with $\lambda = 0.98$ Å) detectors at 90 K. The images were reduced using HKL2000. Both orthorhombic and tetragonal native data sets were collected to 2.5-Å resolution and inhibitor-bound crystal data sets were collected to 3.0 Å resolution (Table I).

Structural analysis

All structures were solved by the molecular replacement method by MOLREP in the CCP4 suite (CCP4, 1994) by using acutolysin-C (1QUA) (Zhu et al, 1999) as a starting model. Initially, the MR solution obtained from the orthorhombic crystal data set, assumed two M-domains in the asymmetric units. After manual rebuilding by TURBO-FRODO, the model was subjected to tortional molecular dynamic refinements with restrained NCS averaging of the M-domains using CNS (Brunger et al, 1998) and iterative refinements and manual rebuilding of the model improved the electron-density map and enabled us to extend the model. First, we found the electron densities associated with the pieces of helical segments of the molecules and modelled them as poly-alanine chains. After cycles of refinements, we assigned those segments as the parts of helices H7 and H8, where the secondary structures are predicted to be helices, judging from the electron densities associated with the side chains. At this stage, four tyrosine residues, Tyr575 and Try576 within the central β strands of the HVRs were clearly defined,

and we noticed that there was another NCS-axis between the C-domains. After iterative rounds of refinements with restrained NCS averaging of the C-domains and manual model building, we completed modelling of the C-domains. From this stage onward, no NCS averaging was included in the refinements. Next, we modelled the D-domains with the help of automated chain tracing using the program ARP/wARP (Perrakis et al, 1999) and with the structural model of trimestatin (1J2L) as a guide. After completely modelling the polypeptide chains, we noticed that isolated lobes of high electron densities surrounded by oxygen atoms occurred both in the D_s- and D_a-domains. For these sites, calcium ions fit optimally to the electron density with a refined occupancy of 100% and reasonably low B-values, thus, we included calcium ions in the model. We also assigned a cobalt ion, which was supplemented in the crystallization buffer for the orthorhombic crystal form, located between the M- and D_s-domains in the A molecule. The part of the carbohydrate chain linked to residue Asn218 (two N-acetyl-glocosamine (NAG) moieties) was modelled. Then, water molecules were assigned. The VAP1 cDNA encodes a protein with 610 amino-acid residues; however, the N-terminus is processed by post-translational modification (Masuda et al, 1998, 2000). Here, protein sequencing of the de-blocked VAP1 molecule clarified that the Glu184 side chain was modified into a pyro-form. The electron densities associated with almost the entire molecule except for the first pyroglutamic acid were defined in either monomer within the orthorhombic crystal. In the final model, 86.1% of the residues lay in the most favorable region, 13.3% in the additionally allowed region and 0.7% in the generously allowed region of the Ramachandran plot. The tetragonal crystal and inhibitor-bound crystal were solved by MR with the domains of the refined orthorhombic apo-form as a starting model. In the final model, 83.6% (80.6%) of the residues lay in the most favorable region, 15.7% (18.9%) in the additionally allowed region and 0.7% (0.5%) in the generously allowed region for tetragonal (inhibitor-bound) crystals in the Ramachandran plot. In either crystal form, the asymmetric unit contained one dimer molecule. All six monomers had almost identical structures. Refinement statistics are shown in Table I.

PDB accession codes

Atomic coordinates and structure factors have been deposited in the Protein Data Bank under accession codes 2ERO, 2ERP and 2ERQ for the orthorhombic native, GM6001-bound form and tetragonal-form, respectively.

Supplementary data

Supplementary data are available at The EMBO Journal Online.

Acknowledgements

References

Almeida EA, Huovila AP, Sutherland AE, Stephens LE, Calarco PG, Shaw LM, Mercurio AM, Sonnenberg A, Primakoff P, Myles DG, White JM (1995) Mouse egg integrin alpha 6 beta 1 functions as a sperm receptor. Cell 81: 1095–1104

Becherer JD, Blobel CP (2003) Biochemical properties and functions of membrane-anchored metalloprotease-disintegrin proteins (ADAMs). Curr Top Dev Biol 54: 101–123

Black RA, Rauch CT, Kozlosky CJ, Peschon JJ, Slack JL, Wolfson MF, Castner BJ, Stocking KL, Reddy P, Srinivasan S, Nelson N, Boiani N, Schooley KA, Gerhart M, Davis R, Fitzner JN, Johnson RS, Paxton RJ, March CJ, Cerretti DP (1997) A metalloproteinase disintegrin that releases tumour-necrosis factor-alpha from cells. Nature 385: 729–733

Blobel CP (2005) ADAMs: key components in EGFR signalling and development. Nat Rev Mol Cell Biol 6: 32–43

Blobel CP, Myles DG, Primakoff P, White JM (1990) Proteolytic processing of a protein involved in sperm-egg fusion correlates with acquisition of fertilization competence. J Cell Biol 111: 69–78

Blobel CP, Wolfsberg TG, Turck CW, Myles DG, Primakoff P, White JM (1992) A potential fusion peptide and an integrin ligand domain in a protein active in sperm-egg fusion. Nature 356: 248–252

Bode W, Gomis-Ruth FX, Stockler W (1993) Astacins, serralysins, snake venom and matrix metalloproteinases exhibit identical zinc-binding environments (HEXXHXXGXXH and Met-turn) and

PRECLINICAL STUDY

Erythropoietin Enhances Neovascularization of Ischemic Myocardium and Improves Left Ventricular Dysfunction After Myocardial Infarction in Dogs

Akio Hirata, MD,* Tetsuo Minamino, MD, PHD,* Hiroshi Asanuma, MD, PHD,* Masashi Fujita, MD,*
Masakatsu Wakeno, MD,† Masafumi Myoishi, MD,† Osamu Tsukamoto, MD,* Ken-ichiro Okada, MD,*
Hidekazu Koyama, BS,* Kazuo Komamura, MD, PHD,§ Seiji Takashima, MD, PHD,*
Yoshiro Shinozaki, MD,‖ Hidezo Mori, MD, PHD,§ Masamichi Shiraga, MD, PHD,‡
Masafumi Kitakaze, MD, PHD, FACC,§ Masatsugu Hori, MD, PHD, FACC*

Osaka and Kanagawa, Japan

OBJECTIVES	We investigated the effects of erythropoietin (EPO) on neovascularization and cardiac function after myocardial infarction (MI).
BACKGROUND	Erythropoietin exerts antiapoptotic effects and mobilizes endothelial progenitor cells (EPCs).
METHODS	We intravenously administered EPO (1,000 IU/kg) immediately [EPO(0) group], 6 h [EPO(6h) group], or 1 week [EPO(1wk) group] after the permanent ligation of the coronary artery in dogs. Control animals received saline immediately after the ligation.
RESULTS	The infarct size 6 h after MI was significantly smaller in the EPO(0) group than in the control group (61.5 ± 6.0% vs. 22.9 ± 2.2%). One week after MI, the circulating CD34-positive mononuclear cell numbers in both the EPO(0) and the EPO(6h) groups were significantly higher than in the control group. In the ischemic region, the capillary density and myocardial blood flow 4 weeks after MI was significantly higher in both the EPO(0) and the EPO(6h) groups than in the control group. Four weeks after MI, left ventricular (LV) ejection fraction in the EPO(6h) (48.6 ± 1.9%) group was significantly higher than that in either the control (41.9 ± 0.9%) or the EPO(1wk) (42.6 ± 1.2%) group but significantly lower than that in the EPO(0) group (56.1 ± 2.3%). The LV end-diastolic pressure 4 weeks after MI in both the EPO(0) and the EPO(6h) groups was significantly lower than either the control or the EPO(1wk) group. Hematologic parameters did not differ among the groups.
CONCLUSIONS	In addition to its acute infarct size-limiting effect, EPO enhances neovascularization, likely via EPC mobilization, and improves cardiac dysfunction in the chronic phase, although it has time-window limitations. (J Am Coll Cardiol 2006;48:176–84) © 2006 by the American College of Cardiology Foundation

Erythropoietin (EPO) is a cytokine that promotes proliferation and differentiation of erythroid precursor cells (1) and is widely used for the treatment of anemia in patients with chronic renal failure (2). Erythropoietin can also exert antiapoptotic and radical scavenger effects on nonerythroid cells (3,4). Indeed, we and others showed that an administration of EPO before or shortly after the onset of ischemia

reduced myocardial infarct size and improved cardiac function in acute phases (5–8). Another interesting nonerythroid function of EPO is the promotion of endothelial progenitor cell (EPC) mobilization in animals and humans

(9–11), which may enhance neovascularization of ischemic areas (12,13). We hypothesized that EPO increases blood supply to ischemic regions through promoting neovascularization and improves cardiac dysfunction after ischemic insult. Thus, the goal of this study was to characterize the effects of EPO on neovascularization and cardiac function after myocardial infarction (MI) in the chronic phase.

METHODS

All procedures were performed in conformity with the Guide for the Care and Use of Laboratory Animals (NIH publication no. 85-23, 1996 revision) and were approved by the Osaka University Committee for Laboratory Animal Use.

Instrumentation. Forty-seven beagle dogs (Kitayama Labes, Yoshiki Farm Gifu, Japan), weighing 8 to 12 kg were used in these experiments. After an intravenous injection of sodium pentobarbital (15 mg/kg), the dogs were intubated and ventilated. General anesthesia was maintained with 0.5% to 2.0% inhaled isoflurane. After baseline echocardiography and hemodynamic assessment, minimal thoracot-

Abbreviations and Acronyms	
ABP	= arterial mean blood pressure
Dil-ac-LDL	= 1,1'-dioctadecyl-3,3,3',3'-tetramethylindocarbocyanine-labeled acetylated low density lipoprotein
EPC	= endothelial progenitor cell
EPO	= erythropoietin
HR	= heart rate
LAD	= left anterior descending coronary artery
LCX	= left circumflex coronary artery
LV	= left ventricle/ventricular
LVEDD	= left ventricular end-diastolic dimension
LVEDP	= left ventricular end-diastolic pressure
MBF	= myocardial blood flow
MI	= myocardial infarction
MNC	= mononuclear cell
UEA-I	= *Ulex europaeus* agglutinin I
VEGF	= vascular endothelial growth factor

omy was performed, and then the left anterior descending coronary artery (LAD) was ligated just distal to the first diagonal branch. To ensure that all animals included in the data analysis were exposed to a similar extent of ischemia, animals with excessive myocardial collateral blood flow (>15 ml/100 g/min) were excluded from study as previously described (14).

Experimental protocols. ACUTE EFFECTS OF EPO ON MYOCARDIAL INFARCT SIZE. Either a single dose of EPO (1,000 IU/kg; 5 ml) (n = 6) or the same volume of saline (n = 6) was administered intravenously immediately after the LAD ligation. Regional myocardial blood flow (MBF), area at risk, and infarct size at 6 h after the LAD ligation were determined as described previously (Fig. 1) (14).

Recombinant human EPO was provided by Chugai Pharmaceutical Co. Ltd. (Tokyo, Japan). Recombinant human EPO is effective for correcting anemia in the beagle dog (15).

EFFECTS OF IMMEDIATE OR DELAYED TREATMENT WITH EPO ON NEOVASCULARIZATION AND CARDIAC FUNCTION. A single dose of EPO (1,000 IU/kg; 5 ml) was administered intravenously immediately [EPO(0) group, n = 8], 6 h [EPO(6h) group, n = 8], or 1 week [EPO(1wk) group, n = 7] after the LAD ligation. Control animals received the same volume of saline (control group, n = 8) immediately after the LAD ligation.

Hematologic parameters. Blood was sampled from a peripheral vein under pentobarbital (15 mg/kg) anesthesia at the time points indicated in Figure 2. Hematologic parameters, including hematocrit, white blood cell count, and platelet count, were measured.

Cytokine measurements. Plasma levels of vascular endothelial growth factor (VEGF) were measured by enzyme-linked immunosorbent assay (R & D Systems, Minneapolis, Minnesota). The detection limit of the assays was 9 pg/ml. The reliability of this assay in dogs has already been reported previously (16).

Quantification of CD34-positive mononuclear cells. The circulating CD34-positive mononuclear cells (CD34+MNCs) were quantified at the time points indicated in Figure 2. In brief, peripheral white blood cells were stained with a phycoerythrin-conjugated anticanine CD34 monoclonal antibody (BD Pharmingen, San Diego, California). Samples were then subjected to a two-dimensional side-scatter-fluorescence dot plot analysis (FACScan, Becton-Dickinson, Tokyo, Japan). After appropriate gating of

A. Experimental groups for acute effects of EPO

1) Control group (n=6) Saline immediately after LAD ligation

2) EPO group (n=6) RhEPO immediately after LAD ligation

B. Experimental protocols for acute effects of EPO
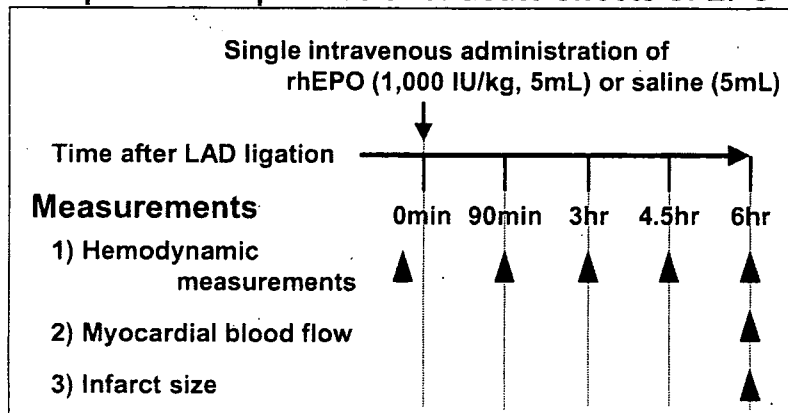
Figure 1. Experimental protocols to investigate acute effects of erythropoietin (EPO) on myocardial infarct size. LAD = left anterior descending coronary artery; RhEPO = recombinant human erythropoietin.